

E-HFWN: Design and performance test of a communication and sensing integrated network for enhanced 5G mmWave[☆]

Chaoyi Zhang ^a, Zhangchao Ma ^a, Xiangna Han ^b, Jianquan Wang ^{a,*}

^a Industrial Internet Institute, Automation and Electronic Engineering College, University of Science and Technology Beijing, Beijing, China

^b Institute of Cultural Heritage and History of Science & Technology, University of Science and Technology Beijing, Beijing, China

ARTICLE INFO

Keywords:

Communication and sensing
Integrated network
5G
6G
mmWave
Air interface technology
Network performance

ABSTRACT

Communication and sensing integrated networks (CSINs) refer to the ability of physical digital space perception and ubiquitous intelligent communication at the same time. These networks realize the perception and cooperative communication of multidimensional resources through the cooperative work of communication and sensing resources and have the ability of intelligent interaction and processing of new information flow. First, this study proposes the technical architecture of an enhanced CSIN (E-HFWN), studies its key technologies and performance indicators, and explains the air interface technology, including frame structure design, carrier aggregation, channel detection, physical skyline mapping, beamforming and management, resource allocation and scheduling. In the resource allocation scheme, an actor-critic reinforcement learning (RL) framework is used to divide the wireless resources. The goal is to maximize the amount of mutual information (MI) and minimize the end-to-end delay of the sensing terminal. Then, the performance of the E-HFWN is tested, including numerical simulation of wireless resource management, system peak rate, capacity, end-to-end delay and communication perception waveform sidelobe ratio. Finally, from the results of the E-HFWN index test, the E-HFWN is further enhanced on the basis of 5G mmWave. The enhanced sensing function can provide a priori information for the optimal and rapid scheduling of distributed computing power and provide richer data sources for artificial intelligence (AI) services and applications to enhance the robustness of the training model. The E-HFWN can contribute to the development of technologies related to 6G synesthesia computing integrated networks, promote the consensus between academia and industry.

1. Introduction

There is a large amount of intelligent automation equipment with highly differentiated capabilities in typical 6G application scenarios represented by smart factories, and the communication requirements for extremely low latency, high reliability, ultralarge bandwidth, and massive access are becoming increasingly stringent. Applications in factories also require high precision and resolution for perception capabilities [1]. On the one hand, the proliferation of wireless communication and sensing devices has made the contradiction between the endless growth of business needs and the limited wireless resources increasingly prominent; on the other hand, the realization of 6G vision requires the acquisition of environment perception information, intelligent information processing, and control closed-loop information flow

processing where information is distributed layer by layer [2]. The existing wireless network architecture and related technologies have been unable to meet the emerging application needs beyond the 5G (B5G)/6G era. It is urgent to develop new network architectures and enabling technologies that efficiently utilize resources and intelligently adapt differentiated applications [3].

In response to the above challenges, research and technological development in academia and industry have great potential [4,5]. On the one hand, in the B5G era, the high frequency bands used by wireless communication networks and the radio sensing frequency bands are gradually approaching or even overlapping [4]; on the other hand, communication and sensing systems have similar characteristics in terms of radio frequency transceivers, channel characteristics, and signal processing, which gave birth to the research and development of

[☆] Chaoyi Zhang, Zhangchao Ma and Xiangna Han are with the University of Science and Technology Beijing, e-mail: (zhangchaoyi@ustb.edu.cn; mazhangchao@ustb.edu.cn; jayna422@126.com). This work is supported by the National Key R&D Program of China (2020YFB1708800, 2020YFC1522404).

* Corresponding author.

E-mail address: wangjianquan@ustb.edu.cn (J. Wang).

synesthesia integrated network architectures and related technologies [5]. In addition, the rise of AI technologies represented by machine learning, RL, neural networks, etc., has had a broad and profound impact in various fields, such as communication network optimization, intelligent perception and control applications, and has promoted the improvement of the overall performance of communication and sensing integration [6].

Based on this, if 6G realizes the integration and symbiosis of communication and sensing capability on the basis of AI technology, it will give 6G networks the ability to perceive the physical world all the time and everywhere. They will not only fully meet the blending and interworking of multidimension intelligent perception of network nodes but also support wide area intelligent cooperation based on communication capability [7], realizing the vision of 6G CSIN. AI services and applications will also be sent to thousands of households with the help of 6G CSIN to help thousands of industries to realize the ubiquitous interconnection of man-machine and objects, intelligent cooperation, and the interaction of the physical world and digital world.

A CSIN refers to a physical digital space perception and ubiquitous intelligent communication. Through the collaboration of synesthesia software and hardware resources, each network element device realizes the deep integration of multidimensional perception and collaborative communication so that the network has the ability of new closed-loop information flow intelligent interaction and processing wide area intelligent cooperation, providing support for 6G smart cities, smart transportation, smart homes and other typical application scenarios [8]. In future intelligent factories, there will be ultradense data interaction applications, which have higher requirements for the throughput and reliability of communication and sensing systems. It is predicted that when the UPF sinks to the edge, 6G networks will need a system throughput performance of 10 Gbps, which will require the mmWave of communication and sensing integration to realize the seamless progress of cooperative communication and environment perception and reduce the signaling overhead [9]. In addition, the integration of communication and sensing for intelligent factories requires a machine end-to-end delay of less than 10 ms, centimeter-level positioning accuracy and reliability of at least 99.999%. These indicators need to further strengthen the air interface design of existing mmWave networks to ensure the application of industrial machines with a large order of magnitude [10]. The contributions and arrangements of this paper are as follows:

- 1) An air interface structure of an enhanced CSIN (E-HFWN) is proposed, including key technologies such as enhanced mmWave frame structure design, system carrier aggregation, wireless channel detection, physical antenna mapping, beamforming and management, system resource allocation and scheduling. These key air interface technologies are further enhanced on the basis of the existing 5G mmWave, especially the frame structure design in the 28 GHz band. The uplink time slot is increased, which greatly improves the transmission efficiency of uplink data. It is especially suitable for uplink data intensive scenarios such as intelligent factories.
- 2) An AI RL method is introduced into the E-HFWN system, which is aimed at the channel resource allocation and scheduling algorithm of communication and sensing. In this study, an actor-critic RL framework is used to divide the wireless resources. The goal is to maximize the amount of MI and minimize the end-to-end delay of the perception terminal.
- 3) Construction and testing of the experimental platform. For the E-HFWN system, this study tests platform performance with communication and sensing. First, the RL is simulated to allocate the communication perception channel resources, and the actor-critic learning framework is fitted from convex optimization theory to achieve the goal of maximizing the MI amount of the system perception signal. Second, the communication performance of the E-HFWN system is tested, including the peak rate, capacity and end-to-

end delay. Compared with 5G and 5G mmWave networks, the enhancement effect brought by air interface technology is compared and analyzed. Then, a sensing performance test of the E-HFWN system is used to calculate the sidelobe ratio of communication and sensing waveform and obtain the peak and integral sidelobe ratio. This result shows that the E-HFWN system has a strong environment sensing ability.

2. Related work

To realize CSIN, the design problem of CSIN air interface technology needs to be solved. To obtain multidimensional perception information, such as the direction, distance and relative motion speed of an environment target, the CSIN can not only realize broadband communication but also receive the echo signal to enhance the perception ability of the carrier array antenna. However, the receiving process of communication signals and perceptual echoes will face problems such as mutual interference and collision. Therefore, it is necessary to carry out the joint optimal design of the CSIN air interface from the aspects of the physical layer, multiple access, wireless resource management and control. On the one hand, physical layer technologies such as the working frequency band, waveform, frame structure design of synesthesia integration and large-scale array antenna beamforming are the basis for the ground application. On the other hand, to solve the problems of mutual interference between communication and sensing signals, research on CSIN multiple access, wireless resource management and control technology is also necessary. In addition, the key technology of the CSIN air interface needs to be verified and evaluated by building an experimental system.

2.1. CSIN spectrum characteristics

The research of this study is in the 28 GHz band, which belongs to the millimeter wave. This band is characterized by large bandwidth and short wavelength. Therefore, the communication rate is faster, the system capacity is larger, and the sensing resolution and accuracy are higher. It is especially suitable for combination with beamforming technology. The direction discrimination ability of beam alignment is better, which is suitable for intelligent factories [11]. In addition, due to the high frequency and long wavelength, it is easy to cause an attenuation phenomenon in the process of electromagnetic wave transmission, which makes the coverage of millimeter waves smaller and based on sight distance. In complex environments, such as industrial sites, more compact, complex physical and MAC layer protocols are designed to compensate for mmWave transmission loss [12,13]. At the same time, a number of hardware terminal devices suitable for the mmWave frequency band have emerged [14], which has laid a solid foundation for the application of CSIN in the mmWave frequency band.

2.2. CSIN channel model

Due to the characteristics of operating in a high frequency band, the CSIN reaches the line of sight (LOS) communication receiving end through one-way propagation, and then the echo signal is reflected by the signal receiving terminal. The echo signal reaches the CSIN transmitting end after the second LOS space loss [15]. In the process of electromagnetic wave transmission, the propagation delay related to the LOS path distance determines the large-scale space loss, and the reflection coefficient (including the radar cross-section parameters of the perceived object) determines the amplitude and phase fading introduced by the signal reflection and scattering process [16]. The propagation delay and reflection coefficient reflect the fading relationship between the spatial sensing channel and single path propagation. Therefore, the key to constructing an integrated communication and sensing channel model under a unified spatial scale and propagation law is ① modeling the twice propagation distance/delay of perception echo

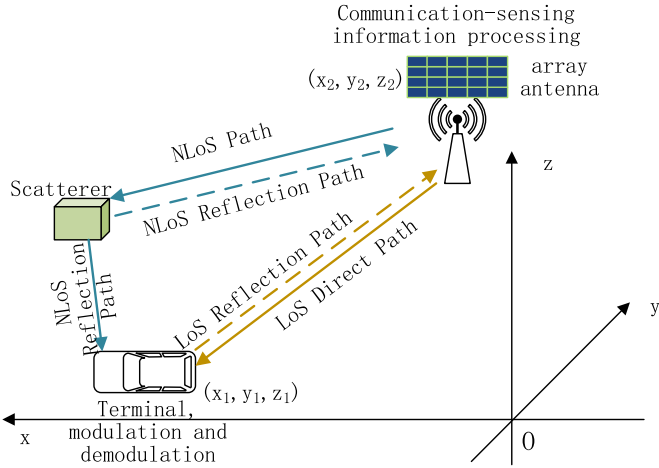


Fig. 1. CSIN correlation channel model.

and ② the relative fading coefficient of the perceptual communication channel generated by additional target reflection. With these two parameters, the CSIN correlation channel model can be constructed [17, 18], as show in Fig. 1.

2.3. CSIN waveform design

At present, the waveform design of the CSIN has three technical routes [19]: ① communication centered integrated waveform design, ② sensing centered integrated waveform design, and ③ communication and sensing combined integrated waveform design.

- 1) The integrated waveform centered on communication realizes the function of perception based on the existing communication waveform. Constant envelope waveform design should be considered so that the perception can transmit signals with a maximum available power budget without signal distortion. It has good correlation characteristics, which minimizes the sidelobe levels of the spatial spectrum and reduces the false detection rate of target detection. In the integrated waveform design scheme based on cellular mobile and Wi-Fi networks, OFDM and FMCW waveforms are combined to improve the resolution and accuracy performance of endogenous sensing to increase the time-bandwidth product [20].
- 2) The integrated waveform design idea centered on sensing embeds communication data into the sensing waveform, to which radar sidelobe beams send digital communication information and operations such as embedding communication symbols in the time/frequency domain of radar waveforms are included [21]. Most schemes use interpulse modulation instead of intrapulse modulation, which results in lower communication rates and spectral efficiency, so radar waveforms are limited to medium/low data rate scenarios [22].
- 3) Unified design of the CSIN waveform from bottom to top provides more flexibility and freedom, for example, in the total transmit power and peak-to-average power ratio (PAPR), it is an integrated waveform design method that minimizes downlink Multi-User Interference (MUI) under the constraints, adds compromise parameters to adjust the priority between sensing and communication system [23]. The difficulty of this design is that the complexity is increased and the hardware is difficult to achieve; it is still in the research stage.

2.4. CSIN frame structure design

Due to the high frequency, the frame structure of the CSIN is more compact and denser. Spectrum characteristics, service requirements, time slot distribution and other contents need to be considered. A frame

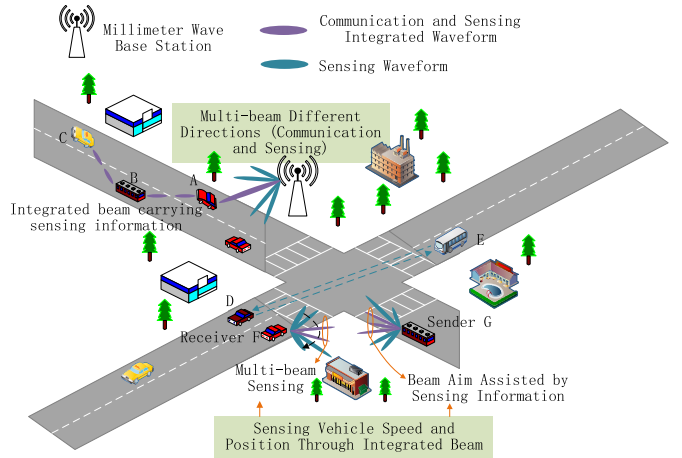


Fig. 2. Schematic diagram of intelligent beamforming integrated with communication and sensing integrated network.

in a period needs to carry more information elements in order to adapt large bandwidth and low time delay, high reliable transmission requirements, and more accurate perception of the surrounding environment [24]. In addition, the frame structure also needs to consider the equipment capabilities of different links, as well as the differences in transmitted signals in the process of beam scanning, beam matching, channel estimation, uplink and downlink data transmission. The design of the overall frame structure is based on these changing needs, resulting in the integration of communication and sensing functions endogenous to the system [25].

2.5. CSIN beamforming technology

The CSIN can realize communication and sensing functions in one direction at the same time by adjusting the alignment direction of the beam. In addition, the system can be combined with beamforming technology to form the direction of multiple beams, which has the function of multiple directions.

Taking the Internet of Vehicles as an example [26], the traditional beamforming method does not define the wireless channel environment and the pointing relationship of the beam, resulting in the beam often failing to aim at the target. A sensor-integrated device can learn the wireless channel environment from the acquired sensor information and then combine with AI technologies such as machine learning to adapt to environmental changes [27], as shown in Fig. 2.

2.6. CSIN wireless resource management

Due to the characteristics of integrated hardware devices (rich and limited resources) and different business types (time delay tolerance and sensitivity), the service requirements for each device or business are also different. To improve the system throughput and spectral efficiency, the management of wireless resources needs to allocate channel resources according to the occupancy status of wireless links, optimization of synesthesia joint performance, and constraints [28].

In future smart factories, the dense access of a large number of terminals will bring the problem of network resource congestion and interference. Under the premise of ensuring the basic CSIN performance constraints of the business, the terminal nodes of dense access can utilize resources in various dimensions to achieve the purpose of optimizing other indicators. For example, reasonable allocation of shared bandwidth for sensing communication, optimization of target positioning performance under power constraints, control power allocation of subcarriers to optimize system performance, etc. [29].

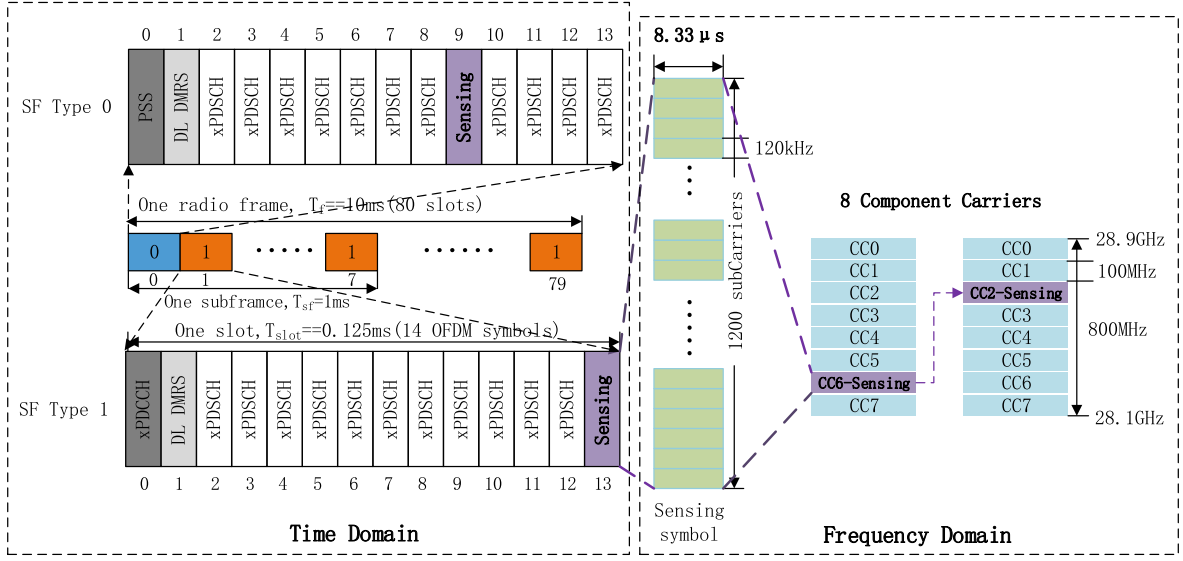


Fig. 3. E-HFWN frame structure.

3. Design of the E-HFWN physical and MAC layer

This chapter focuses on the PHY and MAC layer design of the E-HFWN and introduces two important upgrades to improve the spectral efficiency and system capacity of mmWave communications: optimization on FWA services and DC enhancement. Although the E-HFWN inherits the relevant definitions and principles of the 3GPP R17 version, it does not strictly comply with the 3GPP R17 specification. For example, the E-HFWN introduces n257/n258 frequency band FWA terminal maximum TRP with 23 dBm, multi-RAT DC enhancement, more efficient activation and deactivation features for single SCG and SCell, support for condition PSCell changes and additions, etc.

3.1. Subcarrier bandwidth and frame structure design

The E-HFWN is based on the subcarrier bandwidth and frame structure of 5G mmWave. The frequency range is from 28.1 GHz to 28.9 GHz and has a short data packet design with limited low delay on the MAC layer. The E-HFWN adopts cell topology, the base station (BS) and access points (UEs) are connected, and the 5G carrier modulation is continued based on two waveforms of 802.11OFDM PHY: downlink (DL) waveform (frame from BS to UEs) and uplink (UL) waveforms (frame from UEs to BS). The frame structure is enhanced and varies with the choice of subcarrier spacing. The E-HFWN enhanced frame structure proposed for CSIS is designed based on the 5G NR protocol. The new structure definition is shown in Fig. 3.

Fig. 3 shows the frame structure of the NI mmWave CSIS based on 5G NR. Each frame is consisted with two half-frames, and contains 10 subframes, each subframe contains 8 time slots, of which first time slot is SF Type0, includes the primary synchronization signal (PSS), the other 49 time slots are SF Type1, SF Type0 and Type1 can occupy the frequency domains of sensing and communication functions in time and space, subslot is 0.125 ms, each time slot contains 14-bit OFDM symbols (including CP), the interval of subcarriers is 120 kHz, the duration of each subcarrier is 8.33 μ s, the system bandwidth is 800 MHz, and 8 component carriers (CC) are used, each containing 1200 subcarriers. The system redesigns the Physical Downlink Shared Channel (PDSCH) as a sensing time slot bit and completes the sensing of target location information through a symbol bit. According to the actual service requirements, it can adjust the position and quantity ratio of sensing symbols in the frame structure and achieve efficient utilization of the time-frequency resources required for various functions of communication and sensing.

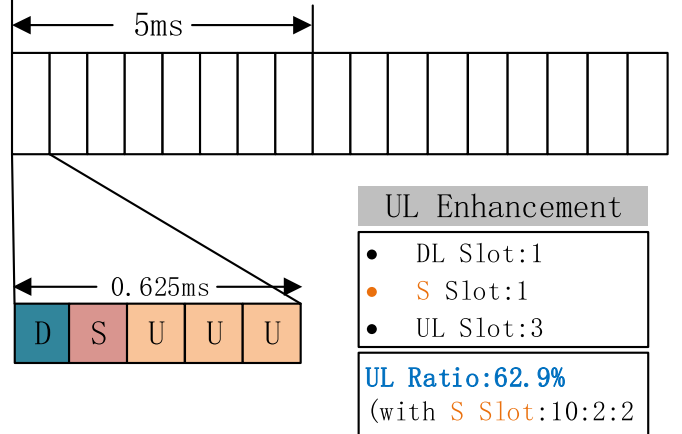


Fig. 4. E-HFWN uplink enhanced frame structure DSUUU (smart factory scenario).

The E-HFWN supports a semistatic or dynamic configuration of uplink and downlink ratios through RRC signaling or DCI scheduling. Most high-frequency frame structures have 5 time slots in one uplink and downlink conversion cycle, as shown in Fig. 4. According to different needs, different uplink and downlink ratios are chosen, among which the pure downlink time slot (marked as D), pure uplink time slot (marked as U), uplink and downlink converted time slot (marked as S). In the S time slot, GP symbols are reserved for uplink and downlink handover, and the number of symbols reserved by GP depends on the time of uplink and downlink handover on the UE side and the planned cell radius.

The design of the E-HFWN frame structure is related to the application scenarios. This research is aimed at the construction of private networks in the field of smart factories. It is used in scenarios where upstream services are dominant, and a large number of terminals, sensing equipment, and industrial video data uploads are used. The dominant frame structure DSUUU has advantages in uplink coverage and capacity.

3.2. E-HFWN carrier aggregation

The DL waveform uses IEEE 802.11's preamble, which is quite large

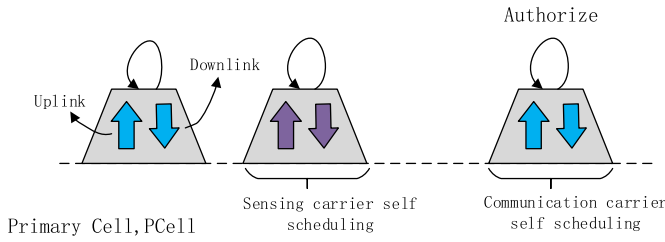


Fig. 5. E-HFVN cell carrier aggregation self-scheduling.

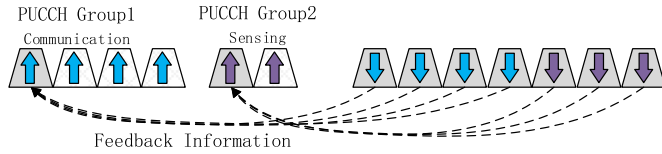


Fig. 6. Allocation of multiple PUCCH groups.

structure; therefore, it is not very effective for communicating short packets. To provide high efficiency, RT data frames sent by UE to different BSs are concatenated into a single frame-through-frame aggregation. The E-HFVN inherits the carrier aggregation function in the NR standard. It can support up to 16 carrier aggregations, so there will be a service bandwidth of $16 \times 400 \text{ MHz} = 6.4 \text{ GHz}$, which exceeds the typical spectrum allocation requirements. These carriers can have different carrier bandwidths or duplex modes.

Starting from the terminal, a terminal that supports carrier aggregation can send and receive data on multiple component carriers at the same time, and a terminal that does not support carrier aggregation can access one component carrier to send and receive data.

In the E-HFVN, due to the business requirements of certain workshops in smart factories, one main cell is set up, and the network can be activated to meet the changes in business requirements. Different terminals are configured in this cell, and uplinks and downlinks can aggregate different carriers (or cells). Due to the frame structure design of Fig. 3, the carrier aggregation needs to be redesigned here. In the carrier component of the E-HFVN frame structure, the communication and sensing component carriers need to be aggregated and scheduled. Since there is only one primary cell, the self-scheduling method is adopted, and the grant and transmission data are sent on the same carrier, but the communication and sensing subcarriers need to be separately processed during self-scheduling, as shown in Fig. 5.

In terms of control signaling, carrier aggregation needs to support Layer 1/Layer 2 uplink control signaling as in the single-carrier case. For example, the gNB needs a terminal to feed back the HARQ confirmation message so that the gNB can know whether the sensing data are transmitted. The design of carrier aggregation is to transmit uplink feedback information in the primary cell, which is convenient to support asymmetric carrier aggregation (the number of uplink and downlink carriers are different in Fig. 4), but in the E-HFVN, the terminals designed for smart factories are configured with multiple uplink carriers, and one downlink carrier is configured. The downlink carrier will carry a large amount of feedback information. To avoid downlink overload, the E-HFVN allows two PUCCH groups to be configured. As shown in Fig. 6, the first group of communication carriers is configured in the downlink primary cell, and the other group is configured in PUCCH as the sensing carrier.

If the aggregated carrier is configured, the terminal can receive or send data on multiple carriers. Therefore, while keeping the carrier aggregation configuration unchanged, the E-HFVN can activate some unused carriers and activate or deactivate component carriers. This is done through MAC layer signaling (MAC control cells).

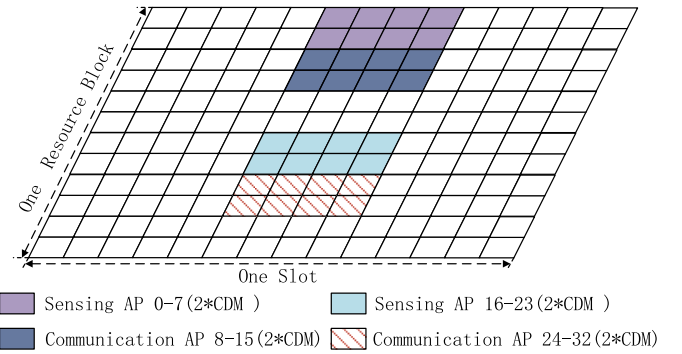


Fig. 7. 32-port CSI-RS support E-HFVN structure.

3.3. Channel detection

To meet the needs of smart factories integrating communication and sensing, the E-HFVN has redesigned the CSI-RS structure under the original NR. An important design principle of NR is to avoid “always on” signals as much as possible. The E-HFVN continues to follow this principle. It keeps the synchronization signal block SSB open and expands the function to better support beam management and mobility as a supplement to SSB.

3.3.1. Downlink channel detection of the E-HFVN: CSI-RS

The downlink CSI-RS structure of the E-HFVN is given. Due to the operation in the 28 GHz frequency band and the description in Sections 3.1-3.2, the CSI-RS supports 32 different antenna ports, and each antenna port is one channel that needs to be detected. mmWave phased array antennas and beamforming are described in Section 3.4.

In the E-HFVN, each terminal can configure the CSI-RS. A set of multiport CSI-RSs can be regarded as multiplexing mutually orthogonal signals on a set of resource unit blocks. The multiplexing method includes CDM, FDM, and TDM. Different CDM methods can be used together with FDM and TDM to support different multiantenna ports (CSI-RS mapping). Generally, a CSI-RS of N ports in one resource block/slot occupy a total of N resource units. The 32-port structure of the E-HFVN is given below, as shown in Fig. 7, which includes 8×CDM, uses 4 times of frequency domain multiplexing at the same time, so that the design cannot occupy continuous subcarriers.

For the downlink channel detection in the 28 GHz frequency band, the 32-port CSI-RS design of the E-HFVN structure, the ports are numbered from the code domain, then the frequency domain, and finally the time domain, as shown in Fig. 7. In the case of 8×CDM, the CSI-RS of 8 adjacent antenna ports are multiplexed together by CDM. For the resource block of FDM + TDM, in Fig. 7, the sensing functions of port groups 0–7 and 16–23 have the same OFDM symbols. The communication functions of ports 8–15 and 24–32 are sent within the same other group with OFDM symbols.

CSI-RS frequency domain structure configuration: The E-HFVN configures CSI-RS in the entire 800 MHz bandwidth. Due to the large number of ports, each resource block is configured with one CSIS-RS, and the density is 3. In the CSI-RS configuration, the information specifies the part of the resource block that carries the communication and sensing, three subcarriers that carry the CSI-RS in one resource block, which are used to track the reference signal configuration.

CSI-RS resource set: The E-HFVN adopts periodic transmission. Due to the strong periodicity of data transmission in smart factories, the transmission period of the CSI-RS is configured as 4, and the time slot offset is 3; that is, the terminal sends every 4 time slots. Then, the CSI-RS can be correctly found where the time domain offset is 3 slots.

Tracking the reference signal: Due to the nonideal nature of the crystal oscillator, the terminal must track and compensate for the reference model in the time and frequency domains to ensure the

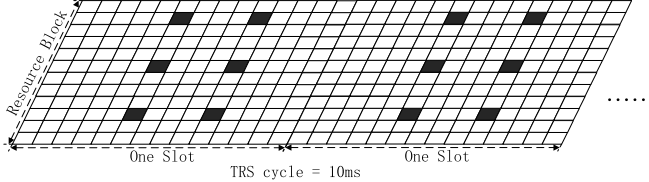


Fig. 8. TRS is distributed in two consecutive time slots, CSI-RS: including 4 single-port, density is set as 3.

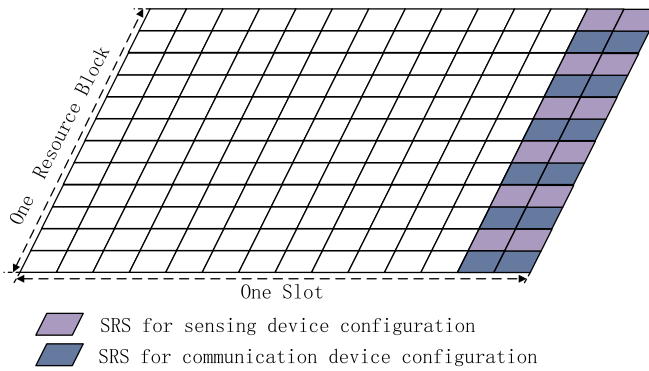


Fig. 9. Communication-sensing terminal multiplexing with two different functions, SRS frequency domain multiplexing structure.

successful reception of downlink data. The E-HFVN tracking reference signal contains 4 single-port CSI-RSs with a density of 3. These CSI-RSs are distributed in two consecutive time slots. As shown in Fig. 8, the CSI-RS in the resource set, that is, TRS, has a period of 10 ms, and the interval between two CSI-RSs is 4 OFDM symbols in each time slot in the time domain. The spacing of the reference signal in the time domain (4 subcarriers) limits the maximum estimable frequency and timing error.

Because the TRS design of the E-HFVN has one antenna port and occupies two time slots in the cycle, the overhead introduced is smaller than that of 5G.

3.3.2. Uplink channel detection of the E-HFVN: SRS

Since the uplink SRS and downlink CSI-RS are both detection channels (different directions), there are similarities. Here, the SRS structure diagram of the E-HFVN is given, as shown in Fig. 9, and the implementation details of the SRS are described.

The E-HFVN continues the SRS structure design idea and places the OFDM symbols of the SRS in the last two positions in a time slot period. In the frequency domain, the SRS selects one subcarrier for every two subcarriers to carry SRS. In addition, according to the communication-sensing integration feature, the SRS signals sent by terminals with different functions will be multiplexed in the same frequency range. For the configuration in Fig. 9, the SRS sent by the communication or sensing terminal will occupy one of the two OFDM symbols so that the frequency domain multiplexing of 2 SRSs can be realized.

SRS sequence and Zadoff-Chu sequence: The design of the E-HFVN transmission SRS sequence is based on the Zadoff-Chu sequence [30]. Since there are many citations about this sequence, it will not be repeated here, but its definition is given:

$$z_i^u = e^{-j\pi u(i+1)} \quad 0 \leq i < M \quad (1)$$

where u is the root index of Zadoff-Chu. For a Zadoff-Chu sequence of fixed length (M , generally a prime number), the root index can generate a unique Zadoff-Chu sequence.

Multiport SRS: The E-HFVN supports multiantenna port channel detection. Different ports can use the same resource unit and SRS sequence. The SRS sequences sent by each antenna port are

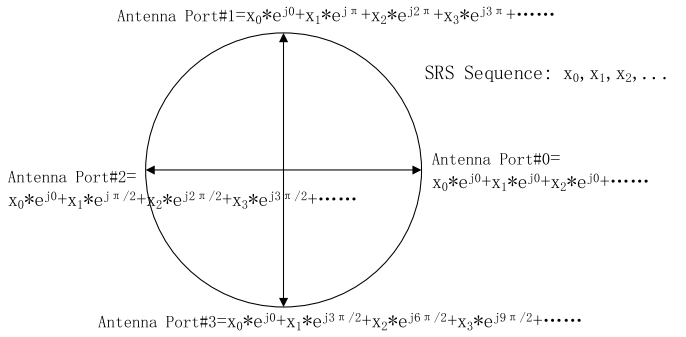


Fig. 10. Different phase rotation of SRS sequence to distinguish multi-antenna ports.

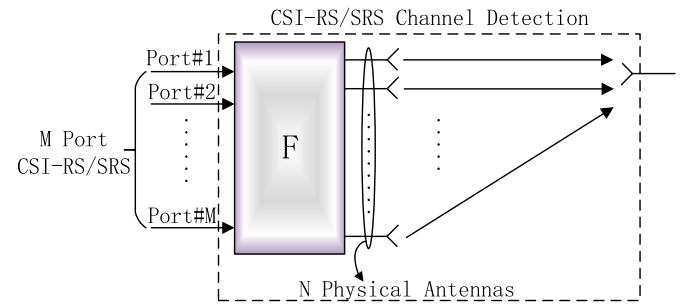


Fig. 11. CSI-RS and SRS are mapped to physical antennas through spatial filter F ($N \gg M$).

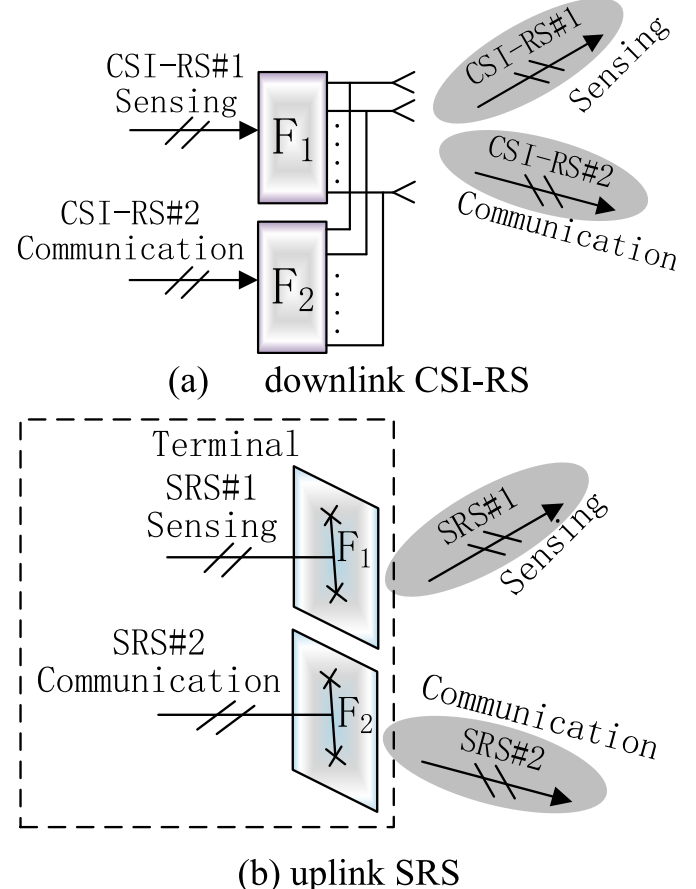


Fig. 12. Different spatial filter F designs for downlink CSI-RS and uplink SRS.

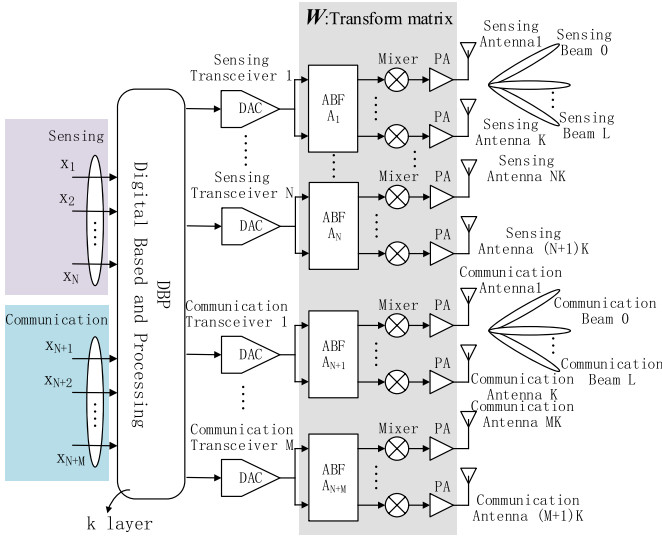


Fig. 13. Hybrid beamforming (analog + digital).

distinguished from each other by phase rotation, as shown in Fig. 10.

SRS resource set: The E-HFWN configures multiple SRS resource sets for communication and sensing terminals. Each resource set contains multiple SRSSs, a single SRS is sent periodically, and the SRS in the resource set must be the same type (such as communication or sensing). The SRS is triggered by DCI signaling in the resource set, which includes 2-bit SRS-request activation transmission.

3.3.3. Physical antenna mapping of the E-HFWN

A multiport CSI-RS or SRS can provide sounding reference signals for channels corresponding to a group of antenna ports. The channels detected by the terminal through CSI-RS or SRS are not wireless channels corresponding to physical wireless. Before the RS is mapped to the physical antenna, a spatial filter F is used to transform the CSI-RS or SRS (linear transformation). The CSI-RS and SRS of the E-HFWN use the same set of logical structure diagrams, as shown in Fig. 11.

From the perspective of the terminal, logical channels (CSI-RS or SRS) of M ports are used for channel estimation, while the N physical antennas and spatial filter F are invisible to the terminal.

The F filters are different for downlink and uplink. In the downlink, the E-HFWN designs a different F for each configured CSIS-RS so that the CSIS-RS beams can be shaped in different directions, as shown in Fig. 12 (a). In this design, although the two CSIS-RSs share the same set of antennas and physical channels, from the perspective of the terminal, two CSIS-RSs are sent through two different channels, and different CSIS-RSs can represent communication ports or sensing ports so that the communication-sensing is separated for channel detection.

In the uplink, the terminal adjusts the direction of multiple antenna panels at a high frequency. At this time, SRS maps the SRS antenna port to a set of physical antennas on the antenna panel through F, and each antenna panel has a different spatial filter, as shown in Fig. 12(b). The advantage of this design is that the transmitted beam has a specific direction or angle in space.

3.4. Large-scale antenna technology (beamforming)

E-HFWN beamforming needs to consider both communication and sensing requirements of network nodes. The sensing function needs to generate a beam scanning effect to achieve a wider range of target detection, while the communication function needs to generate a beam that is aimed at the communication receiver to ensure reliable and stable large-capacity communication. The high frequency band and short wavelength of the 28 GHz mmWave give it a space advantage in design

and deployment, and it is suitable for combining with beamforming technology to enhance performance and reduce interference.

At the high frequency of the E-HFWN, considering a limited number of digital channel MIMO schemes, joint beamforming is performed through digital and analog domains; that is, analog-digital hybrid beamforming technology is used, as shown in Fig. 13. The transmitter (or receiver) consists of multiple subarrays to form an antenna array, where each subarray can steer the beam using an RF phase shifter. In the analog domain, a low-cost phase shifter is used to realize beamforming in a single propagation direction of high-frequency signals; in the digital domain, a baseband processor is used to realize the joint beamforming of multiple propagation directions. Through the CSI feedback of the UE or the measurement of the uplink signal, the weighting coefficient of each array element in the antenna array is adjusted to generate a direction beam so that a significant array gain can be obtained.

The design of transmission matrix W of the E-HFWN is given below: The E-HFWN inherits the design of Release-16 Type II CSI precoder, but here the communication and sensing signals are separated, and we make an enhanced design, import the concept of frequency domain unit to achieve, which supports compressed frequency domain operations. As shown in Fig. 13, given k layers, the precoders of all communication-sensing frequency domain units can be expressed as:

$$[w_k^1, \dots, w_k^N, w_k^{N+1}, \dots, w_k^{N+M}] = W \tilde{W}_{2,k} W_{f,k}^H \quad (2)$$

$$W = W_1 W_2 \quad (3)$$

where N and M are the number of frequency domain units reported by sensing and communication, $[w_k^1, \dots, w_k^N]$ represents the vector set composed of precoders corresponding to all frequency domain units in the sensing layer, $[w_k^{N+1}, \dots, w_k^{N+M}]$ represents the vector set composed of precoders corresponding to all frequency domain units in the communication layer, W is the transfer matrix (matrix dimension is $(N+M)K \times (N+M)$), W is mapped to $(N+M)K$ physical antennas, the output is y , W_1 represents long-term and frequency-independent channel characteristics, the terminal reports one W_1 for the entire reporting bandwidth (bandwidth reporting), W_2 indicates the frequency-related channel characteristics captured in the short term, and the terminal reports one W_2 for each subband. Here, W_1 can be regarded as a beam pointing in a specific direction, which can be expressed as:

$$W_1 = \begin{bmatrix} B & 0 \\ 0 & B \end{bmatrix} \quad (4)$$

where each column of matrix B corresponds to L selected beams, as shown in Fig. 13, Eq. (4) has a 2×2 structure, two diagonal blocks correspond to two polarization directions because W_1 capture long-term and frequency-independent channel information, so the same beam is used in these two polarization directions. At this time, W_1 or B is selected, which actually selects a specific beam from possible beams, so W_1 is actually the beam direction.

To distinguish communication and sensing signals, the E-HFWN sets the rank of matrix W to 2. At this time, W_1 defines four adjacent beams corresponding to four columns of B , so the function of W_2 is to choose which direction to transmit. Since W_2 reports each subband information, the beam direction and interpolarization phase can be adjusted, so W_1 and W_2 can adjust the directions of the sensing and communication beams, respectively.

In E-HFWN-enhanced CSI, it can be seen from Eq. (2) that there are k transmission layers, and there are k precoding vector sets. Each set contains N sensing and M communication precoding vectors. After this design, for a certain frequency domain unit n (sensing) or m (communication), the precoding matrix that maps the transport layer to each antenna port can be obtained, expressed as:

$$W^{(n)} = [w_1^{(n)}, \dots, w_k^{(n)}, w_{k+1}^{(m)}, \dots, w_{k+M}^{(m)}] \quad (5)$$

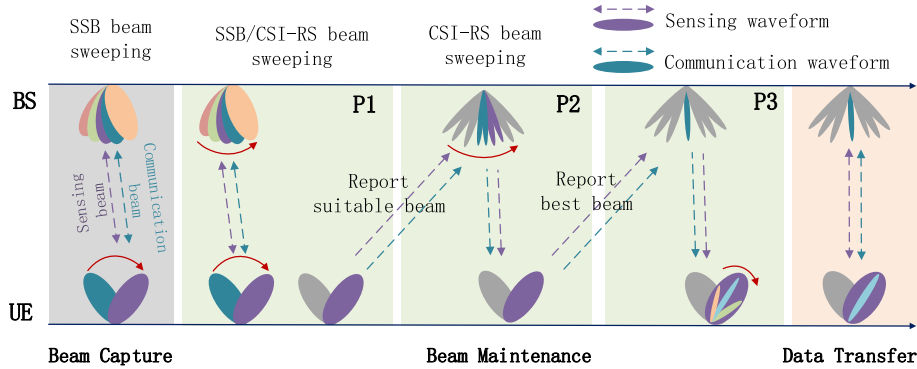


Fig. 14. Communication-sensing beam scanning and tracking process.

The precoding vector corresponding to a specific transport layer is $[w_k^1, \dots, w_k^N, w_k^{N+1}, \dots, w_k^{N+M}]$.

In addition, in Eq. (2), $W_{f,k}^H$ is the enhanced compression matrix introduced by the E-HFWN, and its dimension is $(N+M) \times (N+M)K$. The compression matrix performs DFT on $(N+M)K$ frequency domain units, converts the beam domain into the delay domain, and then selects the smaller $(N+M)$ row value. Since $W_{f,k}^H$ is a frequency-independent matrix, all frequency-domain resource blocks share the compression matrix, and each layer is separately reported. $\tilde{W}_{2,k}$ is a matrix introduced by the E-HFWN to map the delay domain back to the beam domain, and its dimension is $2L \times (N+M)$, which is a different mapping from the frequency domain to the beam domain in Eq. (3), mapping from the time domain can reduce the reporting overhead.

3.5. Beam management

After beamforming in the previous section, it needs to be managed. The beam management of the E-HFWN includes functions such as beam scanning and tracking. The purpose of beam management is to improve the signal transmission gain of BS and UE, increase the data transmission rate, and enhance network coverage. On the one hand, based on integrated synesthesia waveform technology, the dual functions of communication and sensing can be realized by adjusting the beam direction; on the other hand, beamforming technology can also be used to construct multiple beams to achieve the dual functions of communication and sensing in different directions.

To ensure sufficient signal gain, the beam generated by a large-scale antenna array needs to be narrow, and the BS needs to use a large number of narrow beams to ensure that UEs can be covered in any direction of the cell. To align the beam, the E-HFWN adopts a hierarchical scanning strategy, that is, scanning from wide to narrow. Hierarchical scanning can be carried out at any time according to the needs of the terminal, and the optimal beam can be switched with the terminal location. At the same time, to better track UE, beam tracking needs to be used, as shown in Fig. 14.

3.5.1. Beam capture in the access phase

The terminal in the idle state scans the SSB signal in turn to find the SSID¹ with the best signal on the BS and the best receiving beam on the terminal. Then, the terminal sends Msg1 on the RO (Rach Occasion) resource corresponding to this SSID. The BS receives Msg1 and knows which beam to use to communicate with this terminal. The beam corresponding to this SSID is used in the synchronization and access process of subsequent beam capture.

3.5.2. Beam scanning and tracking in the connected state

P1 process: Both BS and UEs use wide beams, the UE performs beam scanning and then informs BS through the CSI report. The wide beam that UE receives from the BS has the best signal quality.

P2 process: In an industrial scene, to meet the traffic requirements of edge terminals, some narrower beams, called refined beams, are designed for remote UEs. Through the P1 process, the receiving beam of the UE is determined, and then through the P2 process, the refined beam is determined. P2 process is that the receiving beam on UE remains unchanged, BS transmits the refined beams in turn, UE informs BS through CSI report, which refined beam has the best signal quality, BS can use refined beam to communicate with UE in traffic channel, to obtain higher gain, this process also called beam alignment.

P3 process: Sometimes high-precision terminals (such as mmWave radars) also have their own refined beams. At this time, the P3 process is used to determine the refined beams used by the terminal. In the P3 process, the transmit beam on the BS remains unchanged, the UE switches the receive beam and then selects the beam with the best signal quality as the beam of the service channel. The beam selection and switching on UE are not perceived by BS.

3.6. E-HFWN resource allocation and scheduling

In the E-HFWN, the focus is the optimization of communication-perception wireless resource management. Millimeter-wave radar can obtain the knowledge map information of targets in medium- and high-frequency bands, such as distance, direction, speed, and attitude. The physical quantity information collected by the E-HFWN is larger than that of traditional sensors, and E-HFWN performance optimization is a multitarget (dual-target) problem that optimizes the performance of perception radar and communication systems. The solution is to obtain the Pareto optimality of the objective function. To maximize the amount of information detected by radar, the E-HFWN can be modeled as a perceptual radar maximization problem with channel capacity. According to Ref. [31], the optimization problem can be defined as:

$$\max_a I_{rad} \quad (6)$$

$$s.t. \quad C1 : a_n \in \Omega_t, \forall n$$

$$C2 : I_i^{sen} \leq I_i^{com}$$

$$C3 : \Delta_i \leq \Delta_i^{max}$$

where I_{rad} represents the total channel MI, which can be expressed as $I_{rad} = \sum_{i=1}^N I_i^{rad}$, and I_i^{rad} represents the i-th communication-sensing channel within the coverage of the BS. The goal of E-HFWN resource optimization is to maximize I_{rad} . $a_n = [a_1, a_2, \dots, a_n]$ denotes the time slot duration sequence of the sensing resource block, n denotes the time index, and Ω_t denotes the set values of a_n , that is, the extent of the slot. In

¹ Communication waveforms, sensing waveforms, communication-sensing integrated waveforms are distinguished by SSID.

a cycle, I_i^{sen} and I_i^{com} represent the perceptual channel capacity and communication channel capacity in the i -th channel, respectively. Δ_i represents the age of information (AoI) of the i -th signal, and Δ_i^{\max} represents the maximum link time. Constraint C1 provides the duration of each sensing terminal, Constraint C2 ensures that the sensing information of each terminal can exist, and Constraint C3 ensures that the data transmission efficiency is lower than a certain threshold when the packet transmission is successful.

In Eq. (6), the channel MI is a measure of the communication and sensing channel. For the convenience of processing in the following algorithm, Eq. (6) can be redefined as:

$$\gamma_i^{\text{rad}} = \rho_{\text{sen}} I_i^{\text{sen}} + \rho_{\text{com}} I_i^{\text{com}} \quad (7)$$

where ρ_{sen} and ρ_{com} are service weight values for distinguishing sensing and communication identifiers, $\rho_{\text{sen}} + \rho_{\text{com}} = 1$, and the service weight value can be adjusted to set the priority of communication and sensing channels [32]. adopts a game theory-based algorithm for Eq. (7). Due to the randomness of indoor perception signals and service requests in smart factories, the actor-critic-based algorithm is adopted in this paper. The RL framework divides the resources of Eq. (7), the goal is to maximize the amount of MI for generating sensing signals and minimize the end-to-end delay of the sensing terminal.

3.6.1. Policy and value function

The allocation strategy is to choose a long-term performance optimization behavior. As mentioned, the industrial scene is complex, and the sensing signal and service request have a certain randomness. Therefore, a random strategy $\pi(a_n|I_i) = \Pr(a_i^{\text{sen}} = a_n | I_i^{\text{sen}} = I_i)$ is adopted for the allocation strategy of MI in the sensing channel; that is, according to the E-HFWN frame structure, the random strategy is determined by the probability distribution of the arrival time in the sensing time slot. The Q-value is defined as starting at time t , the channel MI is I_i , and the time slot duration is a_n , expressed as:

$$Q^\pi(I_i, a_n) = E \left\{ \sum_{k=0}^N \beta^k \gamma_k^{\text{rad}} | \pi, I_i^{\text{sen}} = I_i, a_i^{\text{sen}} = a_n \right\} \quad (8)$$

where $\beta \in (0, 1)$ is the discount factor, and the optimal Q-value is the maximum achievable with optimal action for all decisions. When using this value to estimate the channel state and the optimal Q value of slot permutation (I_i, a_n) , it is necessary to choose greedy permutation to obtain the policy, which is:

$$\pi(a_n|I_i) = \arg \max_{a_n} Q^\pi(I_i, a_n) \quad (9)$$

3.6.2. Value function approximation using a DNN

Due to the large number of subcarriers in the E-HFWN, the channel estimation and time slot allocation dimensions of solving Eq. (9) are high, and the calculation of the channel state and time slot arrangement is expensive. In recent years, due to the progress of machine learning, it has been easy to solve a problem that satisfies a certain law in the probability space, especially when DNN technology is used to approximate the Q-value. Here, $Q^\pi(I_i, a_n)$ is denoted as $Q_w(I_i, a_n)$, the DNN is used to connect multiple hidden layers, and the weight is set as $w = \{w_1, w_2, \dots, w_n\}$. The input layer of the DNN has two units to import systems I_i and a_n into the hidden layer and uses ReLU as the nonlinear activation function. The output of the j -th neuron in the i -th layer can be expressed as:

$$y_{ij} = \max\{0, (w_i \cdot x_i + b_{ij})\} \quad (10)$$

where y_{ij} is the output value, x_i is the input of the i -th layer, w_i is the input weight of the corresponding neuron, and b_{ij} is the bias. The output layer of the DNN provides the estimated Q-value $Q_w(I_i, a_n)$. All that needs to be done is to minimize the loss function and train the DNN to deeply

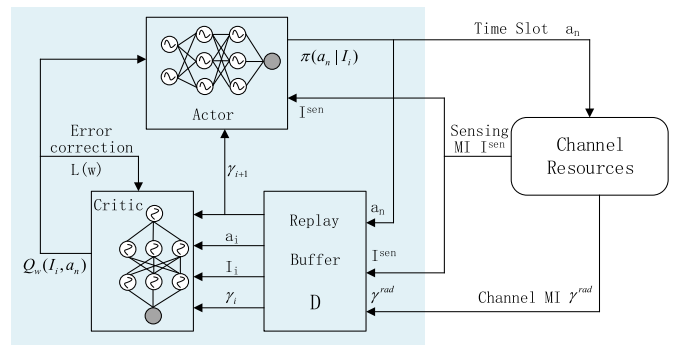


Fig. 15. Actor-critic deep learning-based E-HFWN resource allocation.

learn the best fit weights w .

$$L(w) = E \left[\gamma_i^{\text{rad}} + \beta \max_{a_{n+1}} Q_w(I_{i+1}, a_{n+1}) - Q_w(I_i, a_n) \right]^2 \quad (11)$$

where w is the parameter of the neural network and $L(w)$ is the error value corrected by the DNN. The difference between the target and estimated value is called the adjustment error and is expressed as $\gamma_i^{\text{rad}} + \beta \max_{a_{n+1}} Q_w(I_{i+1}, a_{n+1}) - Q_w(I_i, a_n)$.

For the solution of Eq. (9)~(11), there are:

Critic network: The critic is responsible for the estimation or approximation of the value function, i.e., $Q^\pi(I_i, a_n) \approx Q_w(I_i, a_n)$, the DNN can be used to represent the critic structure in deep RL. However, due to the nonstationarity of the target and correlation between samples, the neural network may cause the RL algorithm to diverge or fail to learn. Therefore, a fixed target network [33] and experience replay [34] are used to establish the critic network to avoid the divergence of the learning algorithm.

Actor network: The actor uses the policy gradient algorithm to evaluate and improve policy, mainly by the agent observing a large number of training samples, among which for a certain signal (such as communication), a higher priority is a positive reward, and a lower priority for another signal (sensing signal) is a negative reward, thereby increasing the probability of network communication and reducing the probability of sensing occurring. Usually, the initialization of the strategy is to design a set of parameters $\theta = \{\theta_1, \theta_2, \dots, \theta_n\}$ and then use another set of parameterized DNNs to represent the actor structure. With the goal of maximizing MI, the strategy is iteratively improved, which is defined as the strategy objective function given by Ref. [35]:

$$J(\pi_\theta) = E[Q^\pi(I_i, a_n)] = \sum_s d(s) \sum_A \pi_\theta(a_n|I_i) Q^\pi(I_i, a_n) \quad (12)$$

where $d(s)$ is the channel state distribution. Partial differentiation of the objective function with respect to the parameter θ can obtain the gradient of the optimal solution and then find the fastest direction of gradient change, which is the final strategy for the actor network solution.

The $L(w)$ of the error calculation can be calculated by the output of the critic network plus the instantaneous channel MI; the process is shown in Fig. 15.

3.6.3. Actor-critic RL algorithm

According to the aforementioned optimization objective and constraint form, as well as the definition of each parameter, the actor-critic RL algorithm is given:

- 1) The actor network initializes random policy $\pi_\theta(a_n|I_i)$, the critic network defines parameterized value function approximation $Q_w(I_i, a_n)$, and both target networks are initialized with random weights θ_i and w_i .

Table 1

Actor-critic deep RL algorithm with communication-sensing resource allocation.

Initialization
Initialization the actor network's θ and its target θ_n ,
Initialization the critic network's w and its target w_n ,
Initialization the error $L(w)_{max}$,
network buffer D
for sample = 1 to S do
set environment channel (com + sen) MI I1, and set
$\gamma_i^{rad} = 0$, $\theta = \theta_i$, $w = w_i$
for time step = 1 to a_{max} do
generate a time slot a_i according to $\pi_\theta(a_n I_i)$
generate subcarrier channel I_i according to $Q_w(I_i, a_n)$
observe sensing MI I_{i+1} and subsequent channel MI
γ_i^{rad} , store the tuple $(I_i, a_n, \gamma_i^{rad}, I_{i+1})$ in D
small batch samples of S-tuples are extracted from D
for $s \in S$ do
if $L(w) < L(w)_{max}$,
update the critic network weight:
$\gamma_i^{rad} + \beta \max_{a_{n+1}} Q_w(I_{i+1}, a_{n+1}) - Q_w(I_i, a_n) + w \rightarrow w$
update the actor network weight:
$\sum_S d(s) \sum_A \pi_\theta(a_n I_i) Q^\pi(I_i, a_n) + \theta \rightarrow \theta$
else $L(w) > L(w)_{max}$
network proceeds to the next iteration
end for
end for

- 2) The actor network is generated at time t, according to current policy $\pi_\theta(a_n|I_i)$ and channel MI's I^{sen} .
- 3) The RL observes the next state of I_{i+1} in sensing channel MI, and γ_i^{rad} in total channel MI stores tuple $(I_i, a_n, \gamma_i^{rad}, I_{i+1})$ in buffer D.
- 4) Randomly sample a mini-batch of S-tuples from the buffer.
- 5) For any sample $s \in S$, the critic estimates the Q-value approximately $Q_w(I_i, a_n)$ and computes the error $L(w)$, indicating whether the (critique) operation (current policy) performs well and updates the parameter w using the mean value of the mini-batch to minimize the loss function.
- 6) For any sample $s \in S$, the Actor uses the output (loss function and estimated Q-value) to calculate the gradient value; at the same time, updates the parameter θ in the direction where the average gradient of the sample changes the fastest to update the output.
- 7) The actor and critic network are jointly allocated resources, and the obtained E-HFVN resource scheduling parameters are updated and it iterates once when $L(w) > L(w)_{max}$, which is the resource allocation rate.

The above algorithm process is written in pseudocode form as shown in Table 1.

4. Numerical simulations

Since the allocation of communication and sensing channels is crucial in the E-HFVN, starting from data acquisition, determines the basis of service quality in the entire system. The actor-critic deep RL algorithm performed numerical simulations. First, parameters are set. When simulating the E-HFVN numerically, the number of BSs is set to 1, and the number of UEs is set to 20, including N communication modules and M sensing terminals, $N + M = 20$. Each time a decision is made, the number of BSs and UEs remains the same, and only the number of carriers for communication and sensing channels changes. Since the service request can be divided into multiple subtasks, the channel can be divided into multiple subchannels and carriers, the communication or sensing ID of each UE can be determined at a specific time (i.e., multiple time slots), and the service of each terminal can be determined. The service request can be regarded as a subcarrier in each time slot, which is mapped to a time-frequency resource block. After this setting, each UE has a fixed service request type in each time slot.

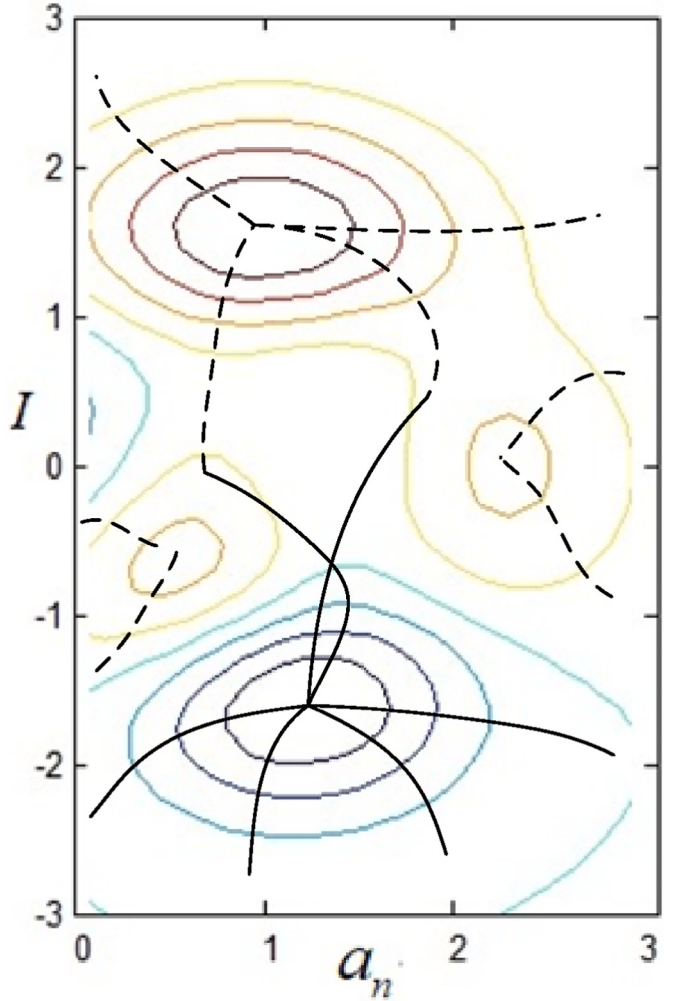


Fig. 16. Algorithm solve trajectories using Standard gradient (dashed) and Natural gradient (solid).

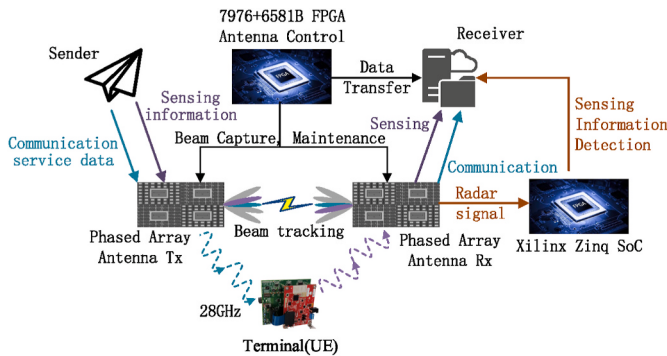
Without loss of generality, the average channel MI is set as {1, 4, 8, 16, 32} in a time slot, where $\gamma = 1$ means MI is the worst, and $\gamma = 32$ means MI is the best. These five channel states allocate time slot resources on MI between UE and BS according to the channel conditions of the industrial field environment. As mentioned above, the total bandwidth is 800 MHz, 8 component carriers (CCs) are used, and each CC contains 1200 subcarriers. When the equipment terminal allocates a CC (communication or sensing channel), the information rate of UE belongs to {1, 2, 3, 4, 5}, the E-HFVN sets a connected DNN, it has two hidden neuron layers, the number of neurons in hidden layer is set as 300, it is verified that the DNN is trained offline at this time, the computational complexity is low. In the actual situation (Chapter 4), the number of neurons is set according to the computational capability of the field terminal. To improve the efficiency of resource allocation and maximize the MI, actor-critic generates two independent training networks. When $L(w) < L(w)_{max}$, the network updates the parameters, sets the size of network data buffer D to 10,000, the sample space S is set as 64, the duration of the time slot sequence is 0.125 ms, a single step is 8.33 μ s, and the service weights of actor-critic are $\rho_{sen} = \rho_{com} = 0.5$.

First, from the numerical simulation results, the mathematical analysis of the channel resource block allocation of the E-HFVN, especially in the optimization strategy of communication-sensing resource allocation, verifies the convergence of the natural gradient ascent method and the standard gradient ascent method. In contrast, the natural gradient ascent method is suitable for the joint optimization of

Table 2

Technical parameters of E-HFWN.

Parameter	Value
Cell radius	10 m
Center frequency	28 GHz
System bandwidth B	800 MHz
Subcarriers	1200
Subcarrier spacing	120 kHz
Duration of subcarrier	8.33us
Noise power spectral	-174dBm/Hz
BER	10^{-4}
BS maximum power	10w
Tx/Rx antenna gain	18 dB
Distance between terminals	<10 m

**Fig. 17.** Testbed architecture of E-HFWN system.

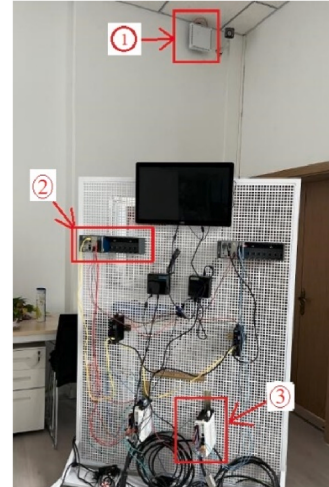
multiple objectives. The resource allocation of communication-sensing channels in the E-HFWN belongs to this optimization problem, while the standard gradient method is suitable for the design of a single optimization objective. The convex optimization modeling graph of $J(\pi_\theta)$ in Eq. (12) uses the natural gradient method (black solid curve) and standard gradient method (black dashed curve) to optimize and solve, as shown in Fig. 16. The horizontal ordinate represents the interval in which the time slot is the step size, and the vertical axis represents the optimized objective function (Channel MI).

It can be seen from Fig. 16 that the actor-critic algorithm can search for the optimal point of the objective function in the steepest ascent direction, near $(1.2, -1.7)$; when using the standard gradient or other optimization methods, the trajectory is deviated for finding the optimal solution in resource allocation, and it obtains $(1.5, 0.9)$, $(0.6, -0.7)$, $(2.2, 0.1)$ and other local optimal points, leading to a decrease in the efficiency of system resource allocation, which cannot meet the needs of multiple services.

5. Results and analysis

The E-HFWN has designed a software simulation platform and hardware test system. Under the premise of the actor-critic-based communication-sensing resource allocation algorithm, the mmWave performance in sections 3.1-3.5 is verified, divided into communication and sensing. The communication indicators include the peak rate, system capacity, and network delay, and the sensing performance indicators include the sidelobe ratio and spatial resolution. Various functional analyses of the built E-HFWN hardware test platform verify the feasibility of the 28 GHz millimeter-wave. Table 2 lists the technical parameters of the E-HFWN system. The transceiver gain of the radar wave antenna is the same as that of the communication system, the main lobe beam width is set to 18 dB, and the transmit power of the communication and radar system is 10 W [36]. The specific system parameters are shown in Table 2.

To meet the coverage requirements of millimeter waves, the E-

**Fig. 18.** Hardware testbed of E-HFWN system (Scene 1).

1. mm-wave RRU and phased array antenna. 2. Terminal controller 3. Terminal 4. Communication-sensing integrated control processing card of E-HFWN 5. feedforward network and interface

HFWN is built in the laboratory environment, and the coverage radius is less than 10 m, so this experiment did not verify the system coverage. Several mmWave radars and communication terminals are distributed in the laboratory. The fading factor of line-of-sight transmission between BS and UE is 2.35. The wireless channel is a frequency selective channel, and the Rayleigh flat fading channel model is adopted.

The E-HFWN realizes the radar detection function in the sensing stage. A set of FPGA hardware test boards is designed to load the E-HFWN frame structure in Section 3.1 based on the 5G NR mmWave frame. The E-HFWN operates on a 28 GHz frequency band and consists of two NI 5G mmWave platforms and two 64-element phased array antennas, as shown in Fig. 17.

The structure of the E-HFWN test platform is shown in Fig. 17, in which both the transmitter and receiver are connected to the phased array antenna. In the working stage, the receiver first operates in radar mode, indicated by the yellow line in the figure. It detects the sensing information and marks the ID in front of the data bit. Then, the communication-sensing integrated FPGA processing board connected to the antenna switches to the communication mode, establishes the Sender→UE→Receiver mmWave link through beamforming and management mechanism designed in sections 3.4-3.5, as shown by purple and blue lines in Fig. 17, and transmits the sensing data in the previous stage of radar mode operation to the receiver side. The final formed field test platform is shown in Fig. 18.

The hardware test bench is shown in Fig. 18. In a laboratory environment, protocol processing center ④ of the E-HFWN is connected to the fronthaul network RRU ① side through southbound interface ⑤. In the RRU, two phased array antennas are connected to the Tx and Rx ends of the radio head as a transmitter and receiver.

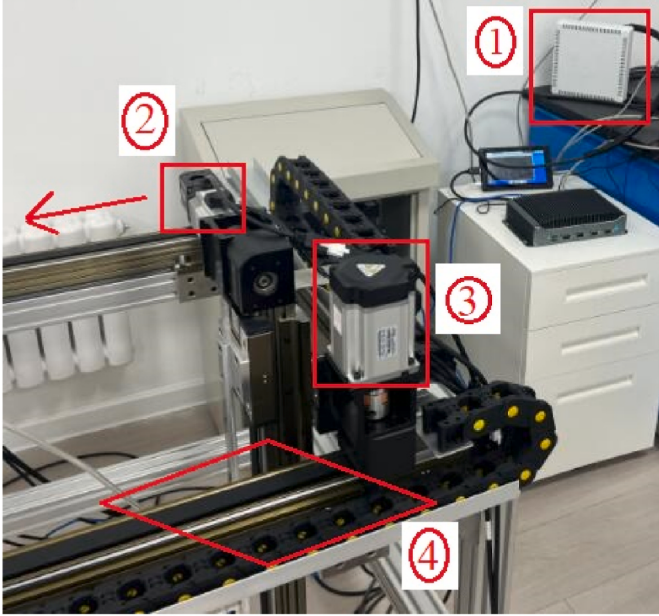


Fig. 19. Hardware testbed of E-HFWN system (Scene 2).

1. mm-wave RRU and phased array antenna. 2. Move slider 3. Electric machinery 4. Guide rail

On the terminal side, it is composed of a mmWave sensor ③ and controller ②. This experiment collects and detects physical quantities such as the number of people, moving trajectories, and speed in the environment space. To test the functions of the mobile terminal for E-HFWN beamforming and management, a set of test field environments are added, as shown in Fig. 19. It is a mobile sliding table. The mmWave sensor can move with the sliding table at a certain speed, and the beam direction will change with the angle of the sensing probe facing antenna ①.

In Fig. 19, the moving speed of slider ② is 0.1 m/s, and the data refresh interval of the mmWave radar is 10 ms. This scenario verifies the ratio of the main lobe and side lobe of the E-HFWN beam and the beam accuracy toward mmWave radar. The receiver Rx performs 4096-point inverse fast Fourier transform (IFFT) processing on the reflected echo. The measurement results show that the moving speed of target ② is 0.0996 m/s, the accuracy is ± 0.0004 m/s, and the detection error of the mmWave is within 0.4%.

5.1. Peak rate of the E-HFWN

In 3GPP TS 38.306, the calculation method for the peak rate is as follows:

$$PR(Mbps)$$

$$= 10^{-6} \cdot \sum_{j=1}^J \left(V_{Layers}^{(j)} \cdot Q_m^{(j)} \cdot F^{(j)} \cdot R_{max} \cdot \frac{N_{PRB}^{BW(j),\mu} \cdot 12}{T_S^\mu} \cdot (1 - OH^{(j)}) \right) \quad (13)$$

where PR represents the peak value rate, J represents the number of carriers, μ represents the order number, $V_{Layers}^{(j)}$ represents the number of space reuse layers, $Q_m^{(j)}$ represents the number of modulation orders, $F^{(j)}$ represents a proportional factor, and R_{max} represents the maximum channel coding rate. $N_{PRB}^{BW(j),\mu}$ represents the total number of PRBs, T_S^μ represents the time for OFDM symbols, and $OH^{(j)}$ represents system overhead. The peak rate of the E-HFWN can be increased by increasing available resources and reducing overhead. The mmWave band is a TDD multiplex, and different TDD frame structure configurations can affect

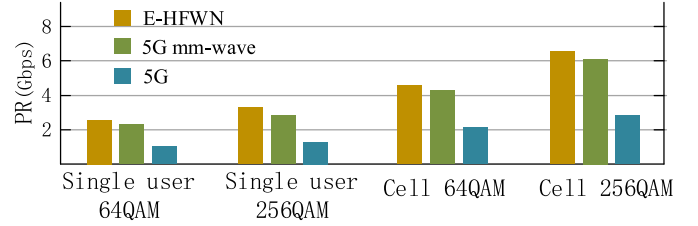


Fig. 20. Downlink PR with same frame structure, different network system and modulation order.

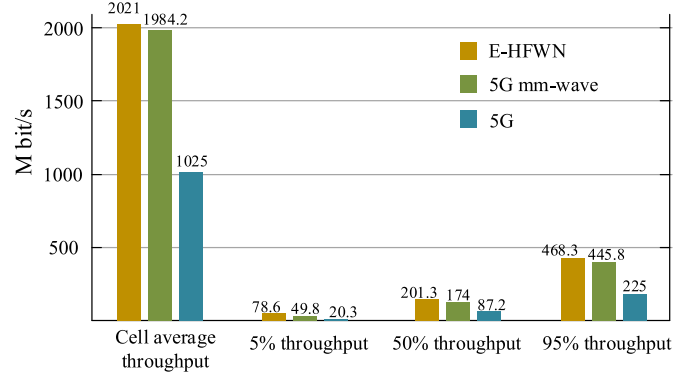


Fig. 21. System capacity under Uma model (coverage radius <50 m).

the uplink peak rate.

According to Eq. (13), this study compares three systems, 5G and 5G mmWave and the E-HFWN, and performs a performance analysis of the UE peak rate and cell peak throughput. The construction and operation of 5G and 5G mmWave systems are in the previous research foundation of our laboratory [37]. For a 28 GHz consecutive 800 MHz bandwidth spectrum, the current single user can support SU-MIMO carrier aggregation transmission of downlink 8×100 M or 4×200 M, uplink 2×100 or 2×200 M. The community can support the uplink and downlink 800 M, 4-run MU-MIMO transmission, and the TDD uplink and downlink timing ratio is 3:1, as shown in Fig. 20.

According to the number of terminals and network services (sensors, controllers, motors, etc.) in the experimental environment, the Monte Carlo service model is used to implement and verify the performance of 5G/5G mmWave/E-HFWN data services, 12 mmWave sectors are deployed in the laboratory environment, and the average number of CPEs with valid service connections is 2 (related to the service activation model) in each sector. As seen in Fig. 20, the more flexible frame structure scheme DSUUU proposed by the E-HFWN is suitable for large uplink services such as factories and laboratories, and it can be allocated according to service requirements to meet service differentiation. The experimental platform shows that the average single-user PR of the E-HFWN can reach up to 2.15 Gbps under 64QAM modulation and 3.5 Gbps under 256QAM modulation; in cell mode, it can reach up to 4.35 Gbps under 64QAM modulation and up to 4.35 Gbps under 256QAM modulation. Up to 6.45 Gbps, the performance of PR is better than that of the 5G and 5G mmWave systems, and the PR of 5G is approximately half that of the E-HFWN, which shows that the mmWave physical and MAC layers designed have been enhanced.

5.2. Capacity of the E-HFWN

For high-frequency network performance, the main indicators are the number of users and average throughput rate of the cell. The number of users can be represented by the number of RRC connected terminals, CAPS and the number of terminals per scheduling period. The cell throughput rate can be calculated from the average and edge throughput

Table 3

Delay parameter of E-HFWN data stream and frame.

Parameters	Meaning
s^i	The packet size of i-th data flow
p^i	The priority of i-th data flow
d^i	Packet interval of i-th data stream
t^i	Start time of i-th data stream sent from terminal A
ts^i	The time that i-th data flow occupies wireless link
$t_{send,j}^i$	The time when j-th packet of i-th data stream is sent from terminal A to BS
$t_{queue,j}^i$	The time when j-th packet of i-th data flow is queued
t_j^i	The end-to-end delay of j-th packet of i-th data flow
$t_{service,j,k}^i$	In kth cycle, the time when j-th packet of i-th data stream is sent from BS to terminal B
$t_{arriveBS,j}^i$	The time when j-th packet of i-th data stream arrives at BS
ρ	Link utilization of BS and terminal
t_{tran}	Send delay
t_{prop}	Propagation delay
t_{proc}	Processing delay

rates. The number of high-frequency terminals is related to the wireless resource configuration of uplink and downlink control channels, which can be analyzed from channel capacity indicators such as PDCCH, PUCCH, and SRS. Similarly, this study verifies and analyzes the network capacity of 5G, 5G mmWave and E-HFWN systems. The capacity comparison results obtained are shown in Fig. 21, where the CPE transmit power is 40 dBm.

The throughput of high-frequency waves is related to the environment and the capabilities of the system itself. Because the network is formed in a laboratory environment, the channel impact of the scene is small, mostly line-of-sight propagation, and the terminal is placed in an obvious space environment. It is distributed where the signal power is stronger; the capability of the system itself includes technical indicators such as system bandwidth, beamforming capability, resource scheduling, and anti-interference. Based on the above conditions, the design of the E-HFWN system has a significant improvement in cell throughput. On the basis of the original 5G mmWave, the system bandwidth is increased, MU-MIMO pairing is optimized, and the MU-MIMO ratio is increased. At the same time, the actor-critic deep learning communication-sensing resource allocation algorithm (section 3.6) improves the efficiency of resource allocation and further improves the cell throughput rate.

5.3. End-to-end delay of the E-HFWN

Another major feature of the E-HFWN is the low end-to-end transmission delay. In 5G, data are scheduled in units of time slots. The shorter the air interface time slot length is, the smaller the transmission delay at the physical layer. The air interface time slot length of the E-HFWN is 0.125 ms, which is 1/4 of the current mainstream 5G medium-and low-frequency systems. Therefore, the E-HFWN is lower than the air interface delay of the 5G/5G mmWave system. The E-HFWN air interface delay measured can be less than 1 ms in the laboratory, which exceeds the service quality requirements of 5G URLLC.

Next, the end-to-end (sensor-to-actuator) delay of the E-HFWN system is analyzed by calculation. The parameter settings of the network data stream (F) and frame (f) are shown in Table 3, $f \in F$.

The above parameters are used to establish data transmission models with different rates, link utilization and queuing delay. To simplify the calculation, the transmission interval of interference flow and BE flow (best effort) is known; then, the delay calculation of each node on the path is as follows:

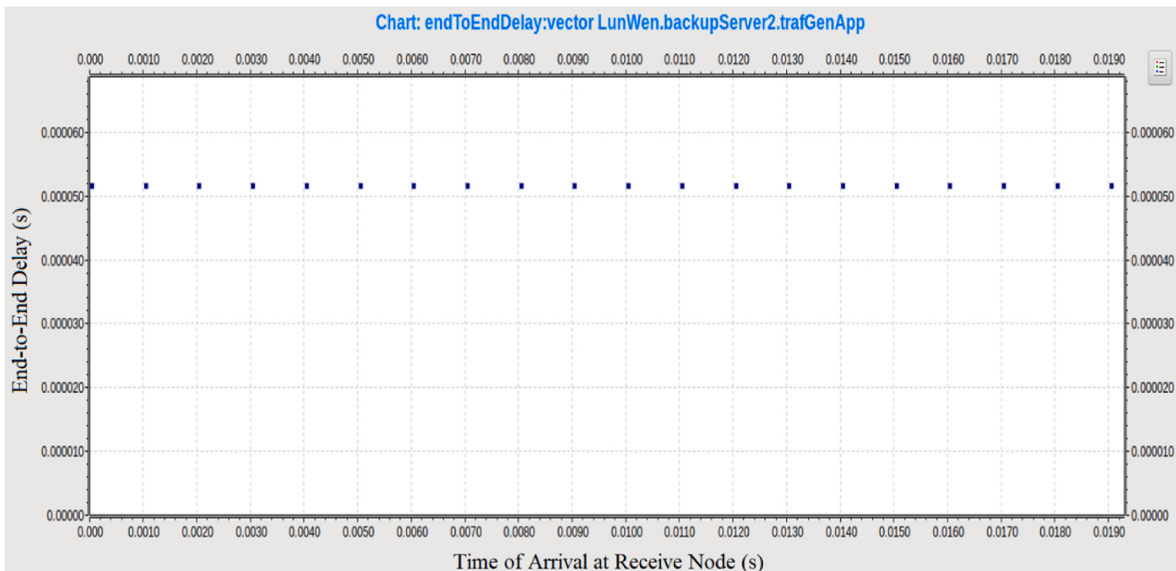
$$t_{arriveBS,j}^i = t_{tran} + t_{prop} + t_{proc} + t_{send,j}^i \quad (14)$$

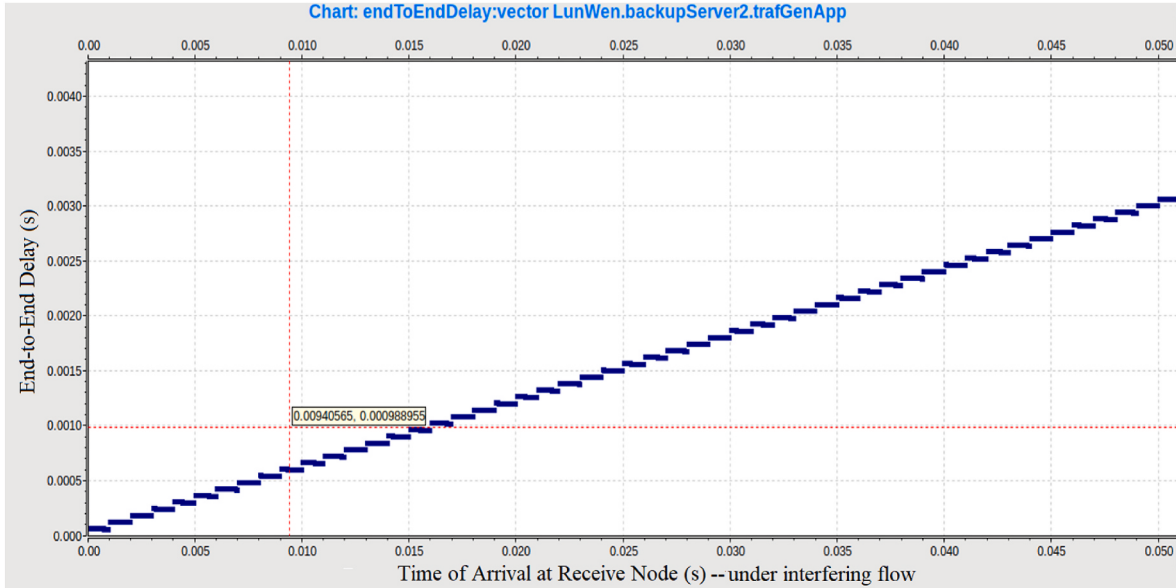
$$t_{tran} = S^i * 8/c \quad (15)$$

$$ts^i = t_{tran} + t_{prop} \quad (16)$$

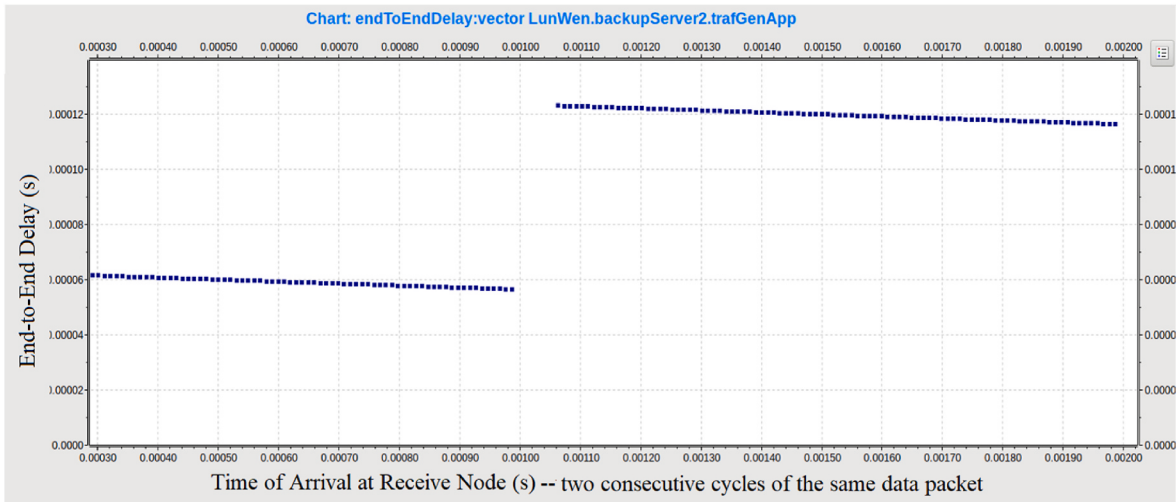
$$t_{send,j}^i = \begin{cases} start_time(j=1) \\ t_{send,j-1}^i + ts^i (ts^i \geq d^i \text{ and } j > 1) \\ (j-1)d^i (ts^i \leq d^i \text{ and } j > 1) \end{cases} \quad (17)$$

For $t_{queue,j}^i$, in the QCI protocol of the E-HFWN, a gate control list is set on the outgoing port of the air interface. In the delay design of the E-HFWN, the time is divided into three time-slot windows: protected window, unprotected window, and guard. In each slot window, a different stream is transmitted. Therefore, for the service flow, if it arrives at the switch at the same time, it is sent according to its priority, and the following variables are set: $0 \sim T_0$ is protected window, which transmits general service flows ($i = 1$), $T_0 \sim T_1$ is unprotected window, transmits BE flow ($i = 2$) and the interference flow ($i = 3$), $T_1 \sim T_2$ is the guard, and all business flows are not transmitted. First, we analyze the transmission in the first cycle, that is, under the condition ($t_{arriveBS,1}^i \leq T_0$):

**Fig. 22.** E-HFWN end-to-end transmission delay without interference.



(a) End-to-end delay under interfering flow conditions



(b) End-to-end delay for two consecutive cycles of the same data packet

Fig. 23. Transmission delay after interference flow is imported into E-HFWN, packet sending interval is 10us.

$$t_{service,j,1}^1 = t_{arriveBS,1}^1 \quad i = 1, \text{ normal QCI service is transmitted} \quad (18)$$

$$t_{service,1,1}^2 = \begin{cases} t_{service,1,1}^1 + ts^1 \cdot t_{arriveBS,1}^2, & t_{service,1,1}^1 + ts^1 > T_0 \\ T_0 \cdot t_{arriveBS,1}^2, & t_{service,1,1}^1 + ts^1 \leq T_0 \end{cases}$$

$i = 2$, Best Effort Business is transmitted (19)

$$t_{service,j,1}^3 = \begin{cases} t_{service,j,1}^2 + ts^2, & j = 1 \\ t_{service,j-1,1}^3 + ts^3 \cdot t_{arriveBS,j}^3, & j > 1 \end{cases}$$

$i = 3$, jamming stream business is joined (20)

Therefore, in one cycle, the queuing delay of various services of the E-HFWN can be obtained:

$$t_{queue,j}^i = t_{service,j,1}^i - t_{arriveBS,j}^i \quad (21)$$

The link utilization in one transmission cycle is:

$$\rho_2 = \frac{ts^1 + ts^2 + j \times ts^3}{T_2} \quad (22)$$

From $t_{service,j,1}^3 < T_1$, $j = n$ is obtained, assuming that $j = n$ is obtained, and n represents the number of frames of interfering streams that BS can process in one cycle when the transmission period for interference flow is a certain value. From this, the delay of the k -th cycle can be obtained:

$$t_{service,1,k}^1 = t_{arriveBS,1}^1 \cdot t_{service,1,k}^2$$

$$= \begin{cases} t_{service,1,k}^1 + ts^1 \cdot t_{arriveBS,1}^2, & t_{service,1,1}^1 + ts^1 > T_0 \\ (k-1) \times T_2 + T_0 \cdot t_{arriveBS,1}^2, & t_{service,1,1}^1 + ts^1 \leq T_0 \end{cases} \quad (23)$$

$$t_{service,j,k}^3 = \begin{cases} t_{service,j-1,k}^3 + ts^3 \cdot t_{arriveBS,j}^3, & j > 1 \\ (k-1) \times T_2 + t_{service,1,k}^2 + ts^2, & j = 1 \end{cases} \quad (24)$$

Similarly, the queuing delay of the E-HFWN in the k -th cycle can be calculated as:

$$t_{queue,j,k}^i = t_{service,j,k}^i - t_{arriveBS,j}^i \quad (25)$$

For multiple cycles of packet transmission, the link utilization is:

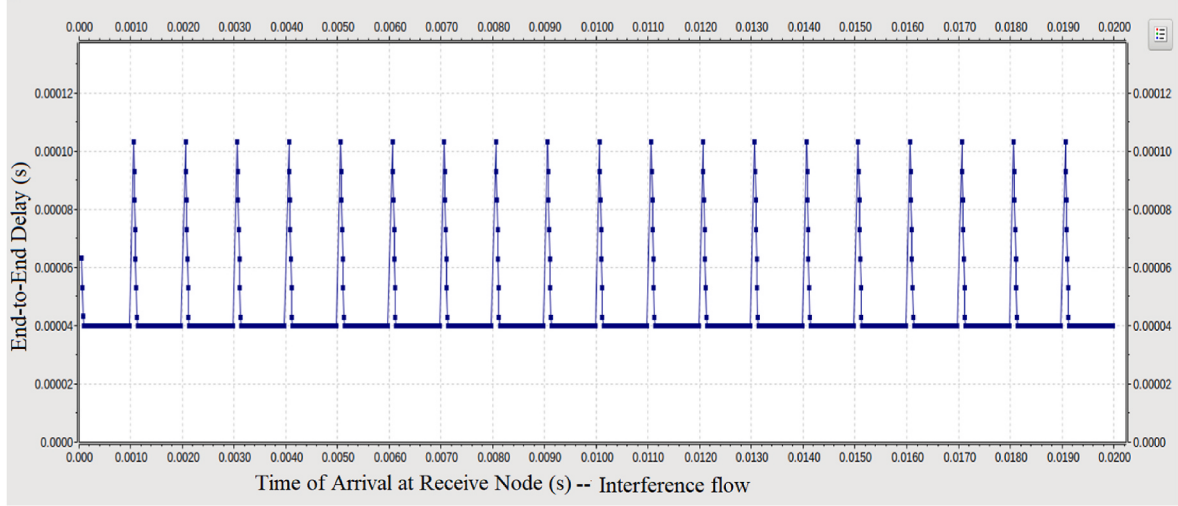
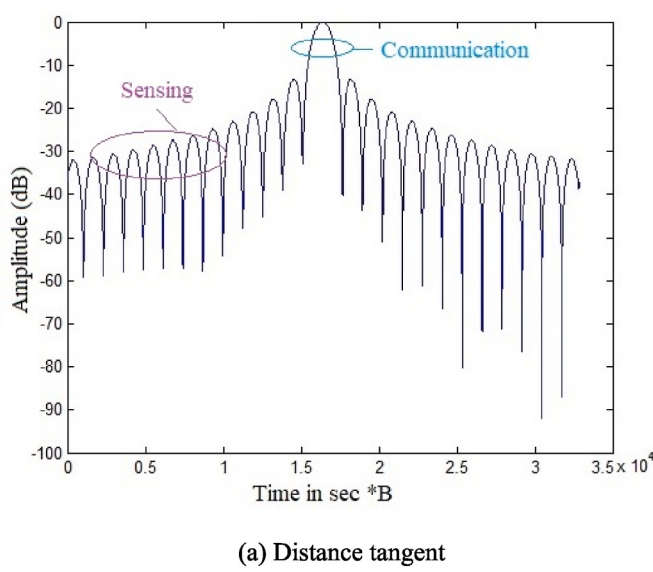
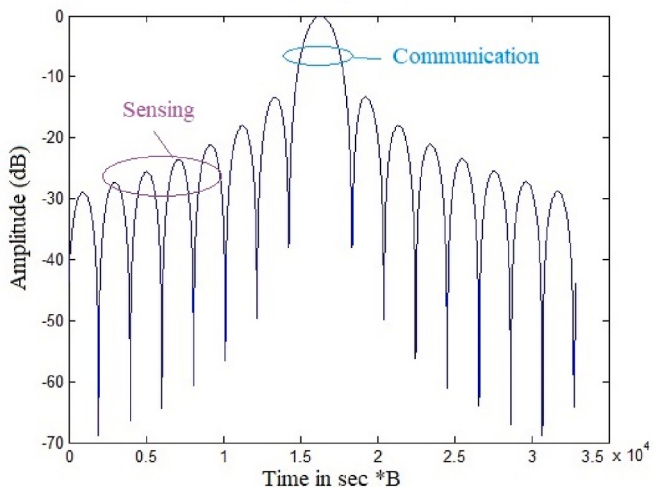


Fig. 24. Interference flow end-to-end delay of E-HFWN (packet sending interval 20us).



(a) Distance tangent



(b) Azimuth tangent

Fig. 25. PSLR and ISLR of communication and sensing signals in E-HFWN (cross-section).

$$\frac{1}{k} \sum_{i=1}^k p_i = \frac{1}{k} \times \sum_{i=1}^k \frac{ts^1 + ts^2 + n \times ts^3}{T_2} = p \quad (26)$$

From this, the relationship between the sending interval of the data packet and its queuing delay and link utilization rate is obtained. Several sets of the E-HFWN end-to-end transmission delay results derived from Eqs. 14–26 are given in Fig. 22, which shows the end-to-end delay of data packets under the condition without interference. The abscissa is the time when the packet arrives at the receiving terminal. The results show that the QCI index of normal services has a large interval for sending packets in time. Under the time slot action mechanism of the E-HFWN frame structure, the end-to-end delay is determined, and there is no interference flow affected.

After the interference flow is imported into the system, it is closer to the actual situation. Since the interference flow has a queuing delay at the BS, Fig. 23 shows the result, and the abscissa is the arrival time at the receiving node. When the packet sending interval is 10 μ s, the generation rate of packets is lower than the service rate of the link, so that the queuing delay of data packets at the BS decreases in each cycle. However, due to the accumulation of data packets in the guard band, there is still a step-up trend in different periods.

Fig. 24 shows the end-to-end delay of interference flow, and the abscissa is the time to reach the receiving node. The results show that when the transmission interval is 20 μ s, the packet generation rate is lower than the link service rate, which makes the queue appear idle for a long time. In this state, the queuing delay of only a few data packets is caused by the scheduling mechanism of the E-HFWN (section 3.6), so that the end-to-end delay of data packets is on the whole in a straight line, with occasional delay oscillations (jitter).

5.4. Communication and sensing beam sidelobe ratios of the E-HFWN

In the environment detection of the E-HFWN, it focuses on the information of the surrounding environment rather than individual targets. The sidelobe ratio performance of communication and sensing beams is important. In radar sensing, the total energy of a single pixel should come from a single spatial resolution. In this section, the peak side lobe ratio (PSLR) and integral side lobe ratio (ISLR) are used to evaluate energy leakage and describe the discrimination between the target and surrounding area. The PSLR and ISLR were numerically fitted to obtain the perceptual performance curve of the E-HFWN under operating conditions, as shown in Fig. 25.

Through the actual test of the E-HFWN, the evaluation indicators of the sidelobe ratio are the point target range and azimuth peak

coordinates, PSLR, one-dimensional ISLR, and two-dimensional ISLR. From Fig. 25 (a), it can be calculated that the range-ISLR of the communication and sensing signal is -9.06 dB, the range-to-PSLR is -12.23 dB, the 3 dB system attenuation bandwidth is 1135 MHz, and the range-direction resolution of the E-HFWN is 0.17. From Fig. 25(b), it can be calculated that the azimuth ISLR of the communication and sensing signals is -9.48 dB, the azimuth PSLR is -12.29 dB, and the 3 dB system attenuation bandwidth is 1821 MHz, which satisfies the system services. At this bandwidth, the range resolution of the E-HFWN is 0.27. The above results meet the performance requirements of communication-perception integration; that is, the E-HFWN system allocates the beams of the communication and perception function so that it can meet the business requirements in general industrial scenarios.

6. Conclusion

Through the deep integration of multi-dimension sensing and intelligent communication, the communication-sensing integrated network enables the network to have high-speed closed-loop information flow transmission, improves spectrum utilization efficiency, and the ability of wide-area intelligent collaboration.

Based on the previous millimeter-wave air interface technology, this paper proposes an integrated system structure of E-HFWN for 28 GHz frequency band, focusing on the enhancement design of key air interface technologies, including frame structure design, carrier aggregation, channel detection, physical antenna mapping, beamforming and management, resource allocation and scheduling key technologies, then this paper introduces intelligent algorithms into the air interface wireless resource allocation scheme to allocate communication and sensing channel resources, minimize the end-to-end transmission delay. Finally, a set of E-HFWN system is built, the communication and sensing performance are tested. The results show that the enhanced E-HFWN has the advantages of capacity, transmission rate, end-to-end delay, and perception of environment physical information. This research result can be used as pre-research basis for 6G and provide a reference for 6G performance evaluation index system. However, the related research on communication-perception integrated network is in its infancy, there are many difficulties and challenges before the technology is mature and commercialized, including: 1) the multi-source information fusion mechanism of communication-perception integrated network; 2) the wireless resources of whole network pooling and efficient deployment methods; 3) communication-perception integrated network efficient configuration, intelligent management and control technology.

Credit author statement

Chaoyi Zhang: Conceptualization, Methodology, Supervision, **Zhangchao Ma:** Investigation, Formal analysis, Writing – original draft, Writing – review & editing, **Xiangna Han:** Physical process analysis, Funding acquisition, **Jianquan Wang:** Project administration, Resources, Funding acquisition.

Declaration of competing interest

The authors declare the following financial interests/personal relationships which may be considered as potential competing interests: Jianquan Wang reports financial support was provided by Ministry of Science and Technology of China. Jianquan Wang reports a relationship with Ministry of Science and Technology of China that includes: funding grants, Xiangna Han reports financial support was provided by Ministry of Science and Technology of China. Xiangna Han reports a relationship with Ministry of Science and Technology of China that includes: funding grants.

Data availability

We have submit our data at 'Attach Files Step'

Acknowledgments

The authors would like to thank the anonymous reviewers for their constructive comments.

References

- [1] Lin JCW, Srivastava G, Zhang YY, Djenouri Y, Aloqaily M. Privacy-preserving multiobjective sanitization model in 6G IoT environments. *IEEE Internet Things J* 2021;8(7):5340–9.
- [2] Huang CW, Hu S, Alexandropoulos GC, Zappone A, et al. Holographic MIMO surfaces for 6G wireless networks: opportunities, challenges, and trends. *IEEE Wireless Commun* 2020;27(5):118–25.
- [3] Zhang Y, Xiao LX, Jiang T. Cloud-based cell-free massive MIMO systems: uplink error probability analysis and near-optimal detector design. *IEEE Trans Commun* 2022;70(2):797–809.
- [4] ITU-T Technical Report. Representative use cases and key network requirements for Network 2030. 2020.
- [5] Raza A, Ijaz U, Ishfaq MK, Ahmad S, et al. Intelligent reflecting surface-assisted terahertz communication towards B5G and 6G: state-of-the-art. *Microw Opt Technol Lett* 2022;64(5):858–66.
- [6] Xiong JB, Zhao MF, Bhuiyan MZA, Chen L, Tian YL. An AI-enabled three-party game framework for guaranteed data privacy in mobile edge crowdsensing of IoT. *IEEE Trans Ind Inf* 2021;17(2):922–33.
- [7] Wang ZQ, Du Y, Wei KJ, Han KF, et al. Vision, application scenarios, and key technology trends for 6G mobile communications. *Sci China Inf Sci* 2022;65(5): 1–27. <https://doi.org/10.1007/s11432-021-3351-5>. 151301.
- [8] Javaid S, Zeadally S, Fahim H, He B. Medical sensors and their integration in wireless body area networks for pervasive healthcare delivery: a review. *IEEE Sensor J* 2022;22(5):3860–77.
- [9] Wang YL, Chen W, Poor HV. Ultra-reliable and low-latency wireless communications in the high snr regime: a cross-layer tradeoff. *IEEE Trans Commun* 2022;70(1):149–62.
- [10] Mahmood A, Beltramelli L, Abedin SF, Zeb S. Industrial IoT in 5G-and-Beyond networks: vision, architecture, and design trends. *IEEE Trans Ind Inf* 2022;18(6): 4122–37.
- [11] Han Y, Shi SJ, Jin RT, Wang YX, Qiu Q. Integrated waveguide true time delay beamforming system based on an SOI platform for 28 GHz millimeter-wave communication. *Appl Opt* 2020;59(26):7770–8.
- [12] Gomez-Cuba F, Zugno T, Kim J, Polese M, et al. Hybrid beamforming in 5G mmWave networks: a full-stack perspective. *IEEE Trans Wireless Commun* 2022;21(2):1288–303.
- [13] Ghaffor S, Boujah N, Rehmani MH, Davy A. MAC protocols for terahertz communication: a comprehensive survey. *IEEE Communications Surveys and Tutorials* 2020;22(4):2236–82.
- [14] Polese M, Jornet JM, Melodia T, Zorzi M. Toward end-to-end, full-stack 6G terahertz networks. *IEEE Commun Mag* 2020;58(11):48–54.
- [15] da Silva JC, Costa E. A ray-tracing model for millimeter-wave radio propagation in dense-scatter outdoor environments. *IEEE Trans Antenn Propag* 2021;69(12): 8618–29.
- [16] Xing YC, Rappaport TS. Millimeter wave and terahertz urban microcell propagation measurements and models. *IEEE Commun Lett* 2021;25(12):3755–9.
- [17] Wu XD, Yang X, Ma SD, Zhou BG, Yang GH. Hybrid Channel estimation for UPA-assisted millimeter-wave massive MIMO IoT systems. *IEEE Internet Things J* 2022; 9(4):2829–42.
- [18] Smith PJ, Senanayake R, Dmochowski PA, Alnajjar KA, Giorgetti A. The impact of channel type on spectrum sensing. *IEEE Wireless Communications Letters* 2022;11(2):230–4.
- [19] Wang XY, Fei ZS, Huang JX, Yu HX. Joint waveform and discrete phase shift design for RIS-assisted integrated sensing and communication system under cramer-rao bound constraint. *IEEE Trans Veh Technol* 2022;71(1):1004–9.
- [20] Ng HJ, Hasan R, Kissinger D. A scalable four-channel frequency-division multiplexing MIMO radar utilizing single-sideband delta-sigma modulation. *IEEE Trans Microw Theor Tech* 2019;67(11):4578–90.
- [21] Bekar M, Baker CJ, Hoare EG, Gashinova M. Joint MIMO radar and communication system using a PSK-1fm waveform with TDM and CDM approaches. *IEEE Sensor J* 2021;21(5):6115–24.
- [22] Shi SZ, Zhao ZY, Liu JN. Comparison of radar waveforms combining pseudo-random binary phase coding and chirp modulation for an high-frequency monostatic radar. *JET Radar, Sonar Navig* 2016;10(5):935–44.
- [23] Dore JB, Gerzaguet R, Cassiau N, Ktenas D. Waveform contenders for 5G: description, analysis and comparison. *Physical Communication* 2017;24:46–61.
- [24] Zhang QX, Wang XN, Li ZH, Wei ZQ. Design and performance evaluation of joint sensing and communication integrated system for 5G mmWave enabled CAVs. *IEEE Journal of Selected Topics in Signal Processing* 2021;15(6):1500–14.
- [25] Lin MT, Xu M, Wan X, Liu HB, et al. Single sensor to estimate DOA with programmable metasurface,. *IEEE Internet Things J* 2021;8(12):10187–97.
- [26] Chen Z, Han C, Wu YZ, Li LX, et al. Terahertz wireless communications for 2030 and beyond: a cutting-edge frontier. *IEEE Commun Mag* 2021;59(11):66–72.

- [27] Maier M, Ebrahimzadeh A, Rostami S, Beniiche A. The Internet of No things: making the Internet disappear and "see the invisible". *IEEE Commun Mag* 2020;58(11):76–82.
- [28] Sun W, Song QY, Zhao J, Guo L, Jamalipour A. Adaptive resource allocation in SWIPT-enabled cognitive IoT networks. *IEEE Internet Things J* 2022;9(1):535–45.
- [29] Heng Yang, Zhiqing Wei, Zhiyong Feng, et al. Queue-aware dynamic resource allocation for the joint communication-radar system. *IEEE Trans Veh Technol* 2021;70(1):754–67.
- [30] Pitaval RA, Popovic BM, Wang P, Berggren F. Overcoming 5G PRACH capacity shortfall: supersets of zadoff-chu sequences with low-correlation zone. *IEEE Trans Commun* 2020;68(9):5673–88.
- [31] Chen L, Liu F, Wang WD, Masouros C. Joint radar-communication transmission: a generalized Pareto optimization framework. *IEEE Trans Signal Process* 2021;69:2752–65.
- [32] Bagheri A, Ebrahimzadeh A, Najimi M. Game-theory-based lifetime maximization of multi-channel cooperative spectrum sensing in wireless sensor networks. *Wireless Network* 2020;26(6):4705–21.
- [33] Mnih V, Kavukcuoglu K, Silver D, Rusu AA, et al. Human-level control through deep reinforcement learning. *Nature* 2015;518(7540):529–33.
- [34] Schaul T, Quan J, Antonoglou I, Silver D. Prioritized experience replay. In: Proc. Int. Conf. Learn. Represent. Puerto Rico: San Juan; May 2016. p. 1–21.
- [35] Bhatnagar S, Sutton RS, Ghavamzadeh M, Lee M. Natural actor-critic algorithms. *Automatica* 2009;45(11):2471–82.
- [36] Yi W, Liu Y, Deng Y, Nallanathan A, Heath RW. Modeling and analysis of mmWave V2X networks with vehicular platoon systems. *IEEE J Sel Area Commun* 2019;37(12):2851–66.
- [37] Sun Lei, Wang Jianquan, Lin Shangjing, Ma Zhangchao, Wei LI, Liang Qilian, Huang Rong. Research on 5G-TSN joint scheduling mechanism based on radio channel information. *J Commun* 2021;42(12):65–75.



ChaoYi Zhang born in December 1985, received his Bachelor's degree in Measurement control technology and instruments from Beijing University of Posts and Telecommunications, Beijing, China, at 2003–2007, received his Master and Ph.D degree in Communication and Information System from Beijing University of Posts and Telecommunications, Beijing, China, at 2007–2012. He worked in Beijing Forestry University as a lecture and associate professor at 2012–2020, Since November of 2020, he worked in University of Science & Technology Beijing as associate professor. His research interests include Communication and sensing integrated network, 5G mmWave, Air interface technology, and he has great interest in 6G technologies.



Zhangchao Ma received his bachelor, graduate and doctor degree in communication engineering from Beijign University of Posts and Telecommunications at 2002–2011, then, he worked in Network Technology Research Institute of China Unicom Research Institute from 2011 to 2017, from 2017–2020, he worked in Guoke quantum communication network Co., Ltd. Since May of 2020, he worked in University of Science & Technology Beijing as associate professor. He is interested in researching in Industrial delay sensitive network, network endogenous security, wireless communication, B5G.



Xiangna Han received her graduate and doctor degree in Institute of Physics and Chemistry from Chinese Academy of Sciences at 2008–2013, then she enter the post-doctoral mobile station of the department of Zhejiang University at 2014–2016. From 2016, she worked in University of Science & Technology Beijing as associate professor. She is interested in physical phenomena in communication systems.



Jianquan Wang received his doctor degree in communication engineering from Beijign University of Posts and Telecommunications at 1998–2003, then he worked in post-doctor workstation in BUPT- China Unicom at 2003–2005, from 2005 to 2017, he worked in Network Technology Research Institute of China Unicom Research Institute, from 2017 to 2020, he worked in Guoke quantum communication network Co., Ltd, Beijing Shenzhou Tianhong Technology Co., Ltd. Since May of 2020, he worked in University of Science & Technology Beijing as professor. He is the leader of scientific and technological innovation of the national “ten thousand talents program”, the young and middle-aged leading talents of the Ministry of science and technology, the expert enjoying the special allowance of the State Council. He presided over and participated in more than 10 special projects, including “863”, NSFC, major projects supported by the Ministry of science and technology, National science and technology major special projects. More than 100 articles have been published, more than 40 invention patents have been authorized; more than 60 international standard manuscripts have been submitted. He is interested in researching in Industrial Internet and heterogeneous network collaboration, network system, key technology and network security.